MCCXXII

UNIVERSITY OF PADUA

DEPARTMENT OF PHYSICS AND ASTRONOMY

Master degree in Astronomy

Hydrodynamic simulations of star formation from molecular cloud collisions

Supervisor: Prof. Paola Marigo
Co-supervisor: Michela Mapelli

Student: Benjamin Czaja
Matricola: 1110266

Abstract

We studied the formation of stars from colliding molecular clouds by performing smoothed particle hydrodynamic (SPH) simulations of six head-on collisions between two molecular clouds with initial velocities of 0, 2, 4, 6, 8 and 10 $\mathrm{km\,s^{-1}}$ respectively. We identify the formation of stars in our simulations by a satisfaction of four criteria: density, overlap, velocity divergence, and binding energy criteria. The accuracy of the criteria was checked by reproducing an initial mass function (IMF) of the formed stars from a single cloud collapse. We also checked that with an increase of resolution in our simulations the mass spectrum produced populated more favorably stellar masses below $2M_\odot$. In the collisions with initial velocities > 2 $\mathrm{km\,s^{-1}}$ we observe that star formation begins after the centers of each cloud have significantly collided. Star formation is initiated earlier as the velocity of the collision increases, while slightly more stars form at lower collision velocities. We also identify 24 star clusters in each of the collisions and observe a linear relationship between the logarithm of the maximum stellar mass in the cluster and the logarithm of the host cluster mass.

Contents

Chapter 1

Star formation in molecular clouds

1.1 Introduction

Star formation in molecular clouds is a complex and important process needed to understand the formation and evolution of our Galaxy along with understanding the origin of stellar and planetary systems. For the scope of this research I will draw out and explain the concepts and current practices behind studying star formation. In this chapter I will give an overview of the physical processes behind star formation and where stars form. In chapter 2 I will discuss the current numerical methods used to simulate star formation. In chapter 3 we perform a smoothed particle hydrodynamic simulation of a single molecular cloud collapse to test our prescription of identifying formed stars. In chapter 4 we simulate and analyze star formation from colliding molecular clouds.

1.2 Location of star formation

The interstellar medium (ISM) is the medium that exists between stars and star systems within a galaxy and is the intermediate region between stellar and galactic scales. The ISM spans a wide range of densities and temperatures; it ranges from cold dense gas (HI or diffuse clouds) with typical densities of 10 cm^{-3} and temperatures below 100 K, to a warm sometimes ionized inter cloud medium with densities of $0.1 - 10$ cm^{-3} and temperatures on the order of 10^3 K, to hot low density regions with densities below 0.01 cm^{-3} and temperatures above 10^5 K [11].

Star formation predominantly occurs in regions of the ISM where molecular hydrogen can form. It is however hard to observe molecular hydrogen directly through emission, as molecular hydrogen is homo-nuclear and has no electric dipole moment. This means that the lowest line transition occurs in the rotational-vibrational $J = 2 \rightarrow 0$ transition, which is faint because of its quadrupole origin [10]. The $J = 2$ state for molecular hydrogen is 511 K above the ground state. Since typical temperatures of regions of molecular hydrogen in the ISM are ≈ 10 K, It is extremely rare to have emission from molecular hydrogen.

Direct detection of H_2 can be observed through ultraviolet absorption, but due to the opaqueness in the ultraviolet band of the Earth's atmosphere these observations must be done from space [36]. A more common indirect observation of H_2 is through radio and sub millimeter emission from dust grains or other molecules close to H_2, which are used as proxies for H_2. One common proxy is observed through the $J = 1 \rightarrow 0$ or $2 \rightarrow 1$ rotational transition of CO [13]. Space and ground based observations have been able to map out the distribution and structures of molecular clouds in the Galaxy and other nearby galaxies. This allows us to better understand and study the process of star formation from molecular clouds.

In this chapter I will outline the location of molecular clouds within the galaxy and their common physical properties in section 1.3. In section 1.4 I will go through the general concepts behind star formation in molecular clouds including Jean's relation, dynamical time, turbulence, and Larson's scaling relations. Finally, I will describe the spectrum of stellar masses that can be formed from molecular clouds in section 1.5. The concepts drawn out in this chapter are the groundwork for the rest of this paper and are key for this research.

1.3 Molecular Clouds

Molecular clouds are interstellar clouds of molecular gas which occupy a small spatial fraction of the ISM, but comprise a large fraction of its mass. Roughly half of the interstellar mass is confined to discrete clouds occupying only ≈ 1 to 2% of the interstellar volume. Molecular clouds tend to appear near the galactic plane and in the spiral arms of galaxies which have been shown by recent surveys of the distribution of CO gas in the Milky Way [13]. Molecular clouds have also been identified and cataloged from CO observations of Milky Way [41]. Shown in figure 1.1 is the distribution of CO gas along the galactic plane. In other spiral galaxies it is observed that molecular clouds trace out spiral arms and galactic disks [26].

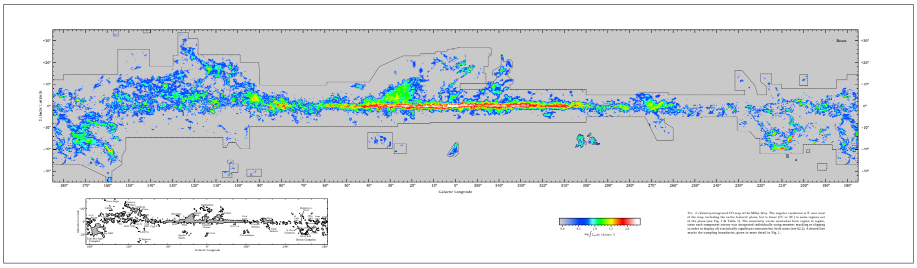

Figure 1.1: A spatial map of the CO gas in the Milky Way integrated over velocity. This shows the large scale distribution of molecular clouds in the Milky Way. The galactic center is identified by its very high intensity, roughly four times that of the surrounding regions.

1.3.1 Structure of molecular clouds

Composed mostly of molecular hydrogen and a small amount of heavier elements, molecular clouds can form stars and star clusters depending on the initial sizes of dense gas clumps within the cloud. Shown in table 1.1 are typical sizes and physical properties of molecular clouds and the kind of systems that can form within them. Star clusters can form from dense clumps within clouds that range from $\approx 0.1 - 10$ pc with temperatures in the range of $10 - 20$ K. Whereas individual protostellar cores can form from dense gas clumps of spatial ranges < 0.1 pc.

Table 1.1: Table of typical sizes and physical properties of molecular clouds and cores. The source of this table is adapted from [5] and [22]

	Molecular cloud	Cluster forming clumps	Protostellar cores
Size (pc)	$2 - 20$	$0.1 - 10$	≤ 0.1
Density ($n(H_2)/cm^3$)	$10^2 - 10^4$	$10^3 - 10^5$	$\geq 10^5$
Mass ($M_\odot$)	$10^2 - 10^4$	$10 - 10^3$	$0.1 - 10$
Temperature (K)	$10 - 30$	$10 - 20$	$7 - 12$
Line width (kms^{-1})	$1 - 10$	$0.3 - 3$	$0.2 - 0.5$
Column density (gcm^{-2})	0.03	$0.03 - 1.0$	$0.3 - 3$
Crossing time (Myr)	$2 - 10$	≤ 1	$0.1 - 0.5$
Free-fall time (Myr)	$0.3 - 3$	$0.1 - 1$	≤ 0.1
Examples	Taurus, Ophiuchus	L1641, L1709	B68, L1544

Molecular clouds above $10^4 M_\odot$ are referred to as giant molecular clouds (GMC)[49]. The typical size of a GMC in the Galaxy is about 10 parsecs to several hundred parsecs, and can range in mass from $10^4 M_\odot$ to $10^7 M_\odot$

[6]. One example of a nearby GMC with active star formation taking place is the Orion A Cloud [18]. A great image illustrating the formation of a new star from the Orion Nebula is shown in figure 1.2. Here we are able to see a new bright star forming in a dense environment in a molecular cloud. Individual molecular clouds exhibit extremely complex filament structures caused by super sonic turbulence. Turbulence can be induced by large scale gravitational motions in the galaxy like spiral density waves, or from more local objects like the momentum transfer from nearby stellar winds [29]. In figure 1.2 we can also see shock fronts caused by the stellar winds from the stars embedded in the cloud.

Figure 1.2: The Orion Nebula is an example of nearby active star formation in a molecular cloud. This close up shows a newly forming star (LL Orionis) providing a shock on the surrounding molecular cloud through its stellar winds. The fast stellar winds with respect to the slow nebular flow create a shock front that is similar to bow shock produced from a boat moving through water. Image courtesy of ESA/Hubble

The overall structure of clouds has clumps and filaments on all scales. Denser clumps of 10^3 cm^{-3} can take up roughly 10% of the total space of a molecular cloud. Even more dense areas of $> 10^5$ cm^{-3} occupy only 0.1% of the spatial structure. But it is important to understand that star formation only takes place in the densest regions of the cloud. This means that most of the molecular cloud material does not form stars and stays at lower densities.

The chemical composition of molecular clouds and the ISM are close to cosmic chemical composition, which can be inferred from measurements from the Sun, and other disk stars in the galaxy. Common chemical compositions are found to be 90.8% hydrogen, 9.1% helium, and 0.12% heavier elements [43].

1.3.2 Timescales of molecular clouds

Molecular clouds occupy a large range of sizes and densities which is reflected by their evolutionary timescales. It is important to understand the typical timescales that govern molecular clouds in order to understand how molecular clouds evolve. The most relevant timescale is the dynamical time, which is the time it will take for a pressure-less sphere of gas to collapse on itself due to gravity. A more detailed derivation is drawn out in section 1.4.2. This timescale defines the behavior of a molecular cloud driven by gravity. There are three important timescales of molecular clouds: the *Gas Depletion Time*, the *Molecular Cloud Lifetime*, and the *Lag Time*.

The *Gas Depletion Time* is the ratio of mass of the molecular cloud to the star formation rate. This is the time it would take to convert the entire mass of the molecular cloud into stars via its star formation rate. The gas depletion time is around a few hundred Myr and is about 100 times larger than the dynamical time. This means that the conversion of gas into stars is inefficient or slow. Only a small fraction of the total mass of a molecular cloud can be converted to stars per dynamical time [25].

The *Molecular Cloud Lifetime* is the actual life time of a molecular cloud. Most of the cloud mass is never converted into stars and remains a part of the cycle of atomic, molecular, and ionized phases of the ISM. This timescale can be found by obtaining age estimates of individual young stars in star forming regions. Since stellar populations older than 0.5×10^7 years are not associated with stellar populations anymore, we expect that the molecular cloud lifetime is much shorter than 10^7 years [19].

Finally the *Lag Time* is the time between the formation of a molecular cloud and when stars begin to form. This can be estimated by taking the ratio of star forming clouds to clouds without significant star formation in the solar neighborhood together with the median age for young stars in these areas. This yields a lag time of ≈ 1 Myr [38]. This very small lag time compared to the molecular cloud lifetime means that molecular clouds start forming stars almost immediately after forming itself.

1.4 Star formation in molecular clouds

Molecular clouds are turbulent self gravitating objects. Understanding the mechanisms behind the formation and birth of stars is necessary for understanding the formation and evolution of our Galaxy. Due to the filamentary structure and large density contrasts of molecular clouds, star formation can happen at the same time in multiple different places in the same cloud. In this section I will give an outline of concepts needed to understand gravitational collapse and turbulence and how it influences star formation.

1.4.1 Jeans length and Jeans mass

We can follow a simple sketch to see how molecular clouds collapse. This is done by assuming that we have a spherical homogeneous dense cloud of gas that has two forces acting on it: a gravitational force acting on the cloud pulling it inwards, and a thermal pressure force from the kinetic energy of the gas particles pushing the cloud outwards. In order to satisfy collapse we must have the condition that in virial equilibrium the gravitational force is more powerful than our internal pressure.

$$|E_{grav}| \geq 2E_{therm} \tag{1.1}$$

Gas particles in our cloud can be approximated as a monotonic ideal gas which allows us to write our kinetic energy as

$$E_{therm} = \frac{3}{2}\frac{M}{\mu m_H}k_B T \tag{1.2}$$

Here M is the mass of the molecular cloud, μ is the molecular weight of the gas, m_H is the mass of the proton, k_B is the Botlzmann constant, and T is the temperature of the gas. We can write the gravitational energy as

$$E_{grav} = -\frac{3}{5}\frac{GM^2}{R} \tag{1.3}$$

Where G is the gravitational constant, and R is the radius of the cloud. Which gives us the condition

$$\frac{GM}{5R} \geq \frac{k_B T}{\mu m_H} \tag{1.4}$$

Using our assumption of a uniform dense cloud we can write the total mass of our cloud $M = \frac{4}{3}\pi\rho R^3$, which allows us to write our condition for collapse in terms of radius.

$$\frac{4}{15}\pi G\rho R^2 \geq \frac{k_B T}{\mu m_H} \tag{1.5}$$

$$R \geq \left(\frac{15k_B T}{4\pi G\rho\mu m_H}\right)^{1/2} \tag{1.6}$$

If the radius of a molecular cloud satisfies this condition it will collapse on itself. This threshold is called the Jeans radius, which was named after the scientist who found this relation in 1919.

$$R_J = \left(\frac{15 k_B T}{4\pi G \rho \mu m_H} \right)^{1/2} \tag{1.7}$$

We can also rearrange this expression for the threshold of the mass. This is called the Jeans mass

$$M_J = \left(\frac{3}{4\pi\rho} \right)^{1/2} \left(\frac{5 k_B T}{G \mu m_H} \right)^{3/2} \tag{1.8}$$

If a molecular cloud has a radius $R \geq R_J$ or a mass $M \geq M_J$ the cloud will collapse under the influence of its own gravity. Notice that both the radius and the mass depend on the physical attributes of the cloud i.e. temperature, chemical composition, and the density. This is a somewhat loose derivation of the Jeans radius and mass. The original derivation follows small perturbations from hydrostatic equilibrium of a spherical cloud of gas [21].

If we do a quick calculation using a molecular cloud with a density of 6.94×10^{-22} gcm^{-3}, a molecular weight of $\mu = 2.46$, and a temperature of 10 K we get a Jeans length of ≈ 0.95 pc. This length is well below the radius of the clouds we use in our simulations (we use clouds with radii of 10 pc). The density used to calculate this Jeans length also comes from the densities we use in our simulations, see sections 3 and 4. Using the same cloud as before we get a Jeans mass of $\approx 37 M_\odot$. Again this is well below our cloud mass, which is $\approx 10^4 M_\odot$. In both cases our clouds exceed the Jeans mass and Jeans radius so they will undergo collapse.

1.4.2 Dynamical time

The timescale at which a molecular cloud collapses or parts of a molecular cloud collapse is called the dynamical time, or free fall time. This is a relatively straight forward concept. We can say that a cloud is in hydrostatic equilibrium when the internal pressure of the cloud is in balance with the self gravitation of the cloud. If the internal pressure suddenly turns off we will have an acceleration at the surface of our cloud due to gravity which can be written as

$$\frac{d^2 R}{dt^2} = -\frac{G M_{cloud}}{R^2(t)} \tag{1.9}$$

with the the initial conditions

$$R(0) = R_{cloud}, \quad \frac{dR}{dt}(0) = 0 \tag{1.10}$$

Therefore the time it will take for the surface of the cloud to fall to $R = 0$ will be

$$t_{dyn} = \left(\frac{\pi^2 R_{cloud}^3}{8GM_{cloud}}\right)^{1/2} \tag{1.11}$$

This is an approximation for the dynamical time. This timescale can be used to estimate how long it will take for the cloud or parts of the cloud to collapse on itself due to the influence of gravity.

We can do a similar order of magnitude calculation as we did before with the Jeans criterion to get an idea of the dynamical time scale. Using a radius of 10 pc and a mass of $4.34 \times 10^4 M_\odot$ we get a dynamical time of 2.5 Myr. This means that the clouds or parts of the clouds that we use in our simulations will collapse under the influence of gravity in ≈ 2.5 Myr.

1.4.3 Larson's scaling relations and turbulence

There exist three basic relations between the parent molecular clouds and the stars that form in them [28]. These relations where found to exist over many scales from dense clumps within clouds, to individual clouds, to entire cloud complexes constisting of many clouds. The relations show how global properties of a cloud are related with *turbulence*, *gravity*, and *density*.

1. **Turbulence:** Velocity dispersion is proportional to cloud size. There exists a power law relationship between velocity dispersion and region size. Regions can range from sizes of entire molecular clouds to smaller components like dense star forming clumps. The relationship follows

   $$\sigma = 1.10\mathrm{kms}^{-1}(L/\mathrm{pc})^{0.38} \tag{1.12}$$

   where L is the size of the regions. The power law follows with an exponent of 0.38. This is close to the prediction of Kolmogrov for turbulence.

   Kolmogorov turbulent flow
   Kolmogorov predicted that the velocity field of in-compressible turbulent flows would be self similar on a range of spatial scales [51]. The similarity on a range of scales results from a dissipation-less cascade of energy from large scales to small scales. In-compressible means that

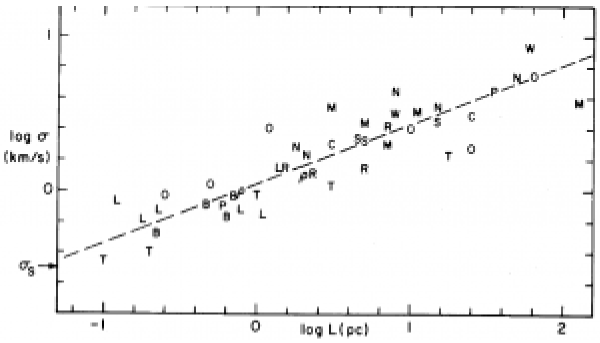

Figure 1.3: The relation between the length of a molecular cloud and its velocity dispersion. The relation follows a slope of 0.38 in logarithmic space. The letters refer to the specific cloud that was measured and the location within the cloud. See [28].

the density of the fluid is homogeneous. Turbulent flows follow the energy spectrum,

$$E(k) = 2\pi k \sum_{i,j} \Phi_{ij}(\vec{k}). \tag{1.13}$$

where the energy spectrum tensor,

$$\Phi_{ij}(\vec{k}) = \frac{1}{(2\pi)^3} \int R_{ij}(\vec{r}) \exp -i\vec{k} \cdot \vec{r} d^3 r \tag{1.14}$$

gives us how much kinetic energy is contained in eddies with wavenumber k.

The length of largest eddies that exist in a turbulent flow is called the correlation length,

$$\Lambda_t = \frac{1}{R(0)} \int_0^{\mathrm{inf}} R(r) dr. \tag{1.15}$$

The smallest eddies exist around the scale called the Kolmogorov or dissipation scale. Turbulent medium is characterized by the mean rate of energy dissipation ϵ_d and the kinematic viscosity η. The dimension of ϵ_d is $\frac{energy}{time \cdot mass}$ and the dimension of η is $\frac{length^2}{time}$. We can rearrange these two quantities to define the Kolmogorov scale,

$$l_K = (\frac{\eta^3}{\epsilon_d})^{\frac{1}{4}}. \tag{1.16}$$

Eddies smaller than this scale will quickly lose their kinetic energy through viscous heating. If a turbulent flow is to be in a steady state turbulent energy must be added, on large scales, at the same rate that it is being dissipated on small scales. The Kolmogorov spectrum is shown in Figure 1.4.

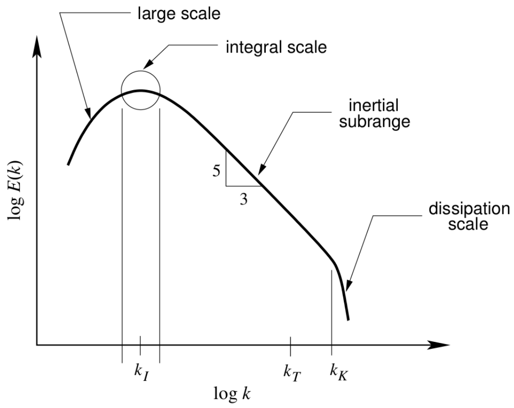

Figure 1.4: The Kolmogorov energy spectrum for an in-compressible turbulent flow. Here we have energy per wave-number k. As the wave-number increases the spatial scale decreases. The integral scale shown here is similar to the correlation length Λ_t.

The power spectrum for representing turbulence in an in-compressible fluid following the form of $E \propto k^{-5/3}$ is generally referred to as the Kolmogorov spectrum. In terms of Larson's scaling relation on turbulence understanding the basics of Kolmogorov's energy spectrum is important.

2. **Gravity:** Velocity Dispersion is proportional to cloud mass. Observed motions show that gravitational collapse in molecular clouds is not a simple radial inward free-fall. It is observed that collapsed regions have irregular, filamentary substructures. Most regions in molecular clouds are in viral equilibrium meaning that they are gravitationaly bound but also in balance with the internal energy of the cloud. This balance exists because of turbulent internal velocities that are supporting the cloud from collapse. Turbulent velocity fields cause these filamentary structures in collapsed regions. In Figure 1.5 we see a relation between a molecular cloud's mass and its velocity dispersion.

   The relation between the mass of a cloud and the velocity dispersion is found to follow
   $$\sigma = 0.42\text{kms}^{-1}(M/M_{\odot})^{0.2}. \tag{1.17}$$

3. **Density:** Cloud size is inversely proportional to density. This scaling law can be thought simply as a result of the first two laws being correct.

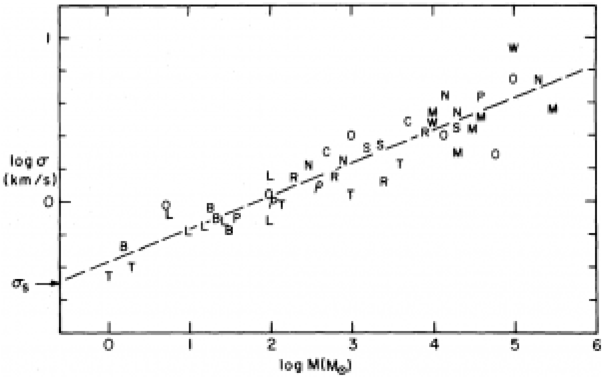

Figure 1.5: The scaling relation between the mass of a molecular cloud and its velocity dispersion σ. Here we view the relation in logarithm space, with a trend of the slope $\propto 0.2$. The letters refer to the specific cloud that was measured and the location within the cloud, see [28].

We can see this relation by simply following dimensional analysis of density. We saw that length is scales with velocity dispersion and that velocity dispersion scales with mass in both laws one and two, i.e. $\sigma \propto L^{0.38}$ and $\sigma \propto M^{0.2}$. This can lead us to say $L \propto M^{0.52}$ or $M \propto L^{1.9}$. We just use the expression for density $\rho = \frac{M}{L^3}$ to find that density is inversely related to length as $\rho \propto L^{-1.1}$.

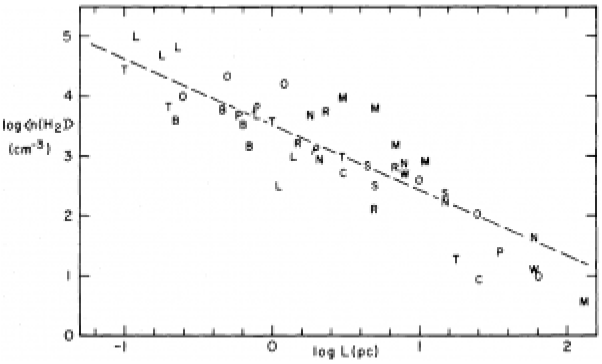

Figure 1.6: The relation between the density of a molecular cloud and its size. The letters refer to the specific cloud that was measured and the location within the cloud, see [28].

This relation was measured by Larson and will follow more closely the relation,

$$< n(H_2) >= 3200\text{cm}^{-3}(L/\text{pc})^{-1.1}. \qquad (1.18)$$

> We can see the result shown in Figure 1.6. Larson also showed that when measuring the column density of the molecular cloud there was no dependence on the size of the cloud. This makes sense since column density is the density of the cloud times cloud length. So if we return to dimension analysis we will expect no relation between column density and cloud length.

1.5 The initial mass function

A common tool for investigating the population of stars that are born from a molecular cloud is the initial mass function (IMF). An IMF is the spectrum of masses that stars have when they are born. More precisely the IMF is a mass spectrum of stars when they enter the zero age main sequence. The IMF alternatively can also be thought of as a probability function predicting the mass that a star might have when it forms. The IMF can be a powerful tool for star formation studies using simulations because it is an observable that can be reproduced to see if the simulation is physically accurate. The IMF was introduced in 1955 by E. Salpeter as a power-law and has the form

$$\Phi(\log m) = dN/d\log m \propto m^{-\Gamma} \tag{1.19}$$

Or more commonly written as

$$dN \propto m^{-\Gamma} d(\log m). \tag{1.20}$$

Here m is the mass of an individual star, and N is the total number of stars within some logarithmic mass range $\log m + d\log m$. It shows that the number of stars formed decreases as the mass range increases. When first introduced the IMF followed a single power law with a logarithmic slope of $\Gamma \approx 1.35$ [42]. Salpeter found a rate of star creation as a function of stellar mass from observing the luminosity of main sequence stars in the solar neighborhood. The single power law IMF with a slope of $\Gamma = 1.35$ is commonly referred to as the Salpeter IMF, and will be used throughout this paper. However, the IMF and its universality are currently debated. It may vary depending on the environment, but can be more or less invariant.

More recent studies have revealed that the IMF may not be described by a single power law but might follow a segmented power law. A multi-segmented power law was later introduced by measuring the distribution of low mass stars in the Galactic disc. These indicate the slope of the IMF at lower masses is shallower than value obtained for higher masses [23]. This segmented power law is commonly referred to as the Kroupa IMF after the scientist that proposed it.

The IMF can also be written in terms linear mass units in the context of a mass spectrum.

$$dN/dm \propto m^{-\alpha} \tag{1.21}$$

This allows us to estimate the number of stars in a given mass range. We can relate the two versions of the IMF written in logarithmic units and in linear units by following the logarithmic relation

$$dN/dm = 1/(m \ln 10)\Phi(logm) \tag{1.22}$$

Which allows us to equate our exponents describing the slope of the IMF.

$$\alpha = \Gamma + 1 \tag{1.23}$$

We chose in this paper to follow equation 1.21 to present the initial mass function. The Salpeter IMF follows a slope of $\alpha = 2.35$. And the Kroupa IMF follows a segmented slope of $\alpha = 0.3$ for $m < 0.08M_\odot$, $\alpha = 1.3$ for $0.08M_\odot < m < 0.5M_\odot$, and $\alpha = 2.3$ for $0.5M_\odot < m$. In figure 1.7 we see both mass functions plotted together. The 3rd IMF plotted in figure 1.7 is the Chabrier mass function, which was discovered by looking the mass spectrum from various components of the Galactic disk, spheroid, young, and globular clusters. [8].

There are three main approaches to observe the IMF. The most direct approach is to measure the mass of the population of stars in a young cluster where stars are coeval and individual stellar masses can be measured down to low masses [37]. However, the number of young clusters limits the statistics of this usually clean measurement. Another method is to measure field stars in the Solar neighborhood which are no longer in clusters. This will give us better statistics but will limit us to low mass stars. We cannot use the high mass stars in the solar neighborhood because the population of high mass stars close to the Sun is highly determined by the star formation rate rather than the IMF. This method was the one used by Salpeter. The final common measurement of the IMF is done through integrating light from stellar populations [32].

1.6 Cluster mass as an upper limit to stellar mass

Finding an upper limit to stellar masses is a current topic in stellar evolution. The first theoretical upper limit on the stellar mass was put forward by Arthur Eddington who calculated the mass limit that was required to balance

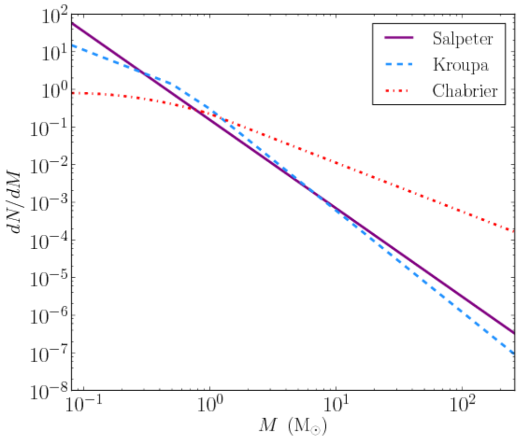

Figure 1.7: An example of multiple initial mass functions plotted together, logarithm of number of stars per mass bin dN/dM per logarithm of stellar masses $N(M_*)$. The solid purple line is the Salpeter IMF, with a slope of $\alpha = -2.35$. The dashed light blue line is the Kroupa IMF, with a segmented slope of $\alpha = -0.3$ for $m < 0.08M_\odot$, $\alpha = -1.3$ for $0.08M_\odot < m < 0.5M_\odot$, and $\alpha = -2.3$ for $0.5M_\odot < m$. The dashed red line is the Chabrier. For $m < 1$ $M_\odot$ $dN/dm = 0.158(1/m)\exp - \log m - \log 0.08^2/(2 \cdot 0.69^2)$. For $m > 1M_\odot$ $\alpha = -2.3$. Figure adapted from [12]

the inward gravitational pull with the outward radiation pressure, called the Eddington limit [14]. In other words hydrostatic equilibrium of a star would fail if the mass exceeded $M \approx 60M_\odot$. However massive stars are not fully radiative and have convective cores which can lead to masses exceeding $60M_\odot$. Stellar masses of $120 - 150M_\odot$ have been found to be possible due to a damping of their pulsations [45], [3]. Formation models suggest maximum stellar masses of $40 - 100M_\odot$ due to the feedback of the protostellar system on the surrounding spherical accretion envelope [50].

However observational limits on an upper limit of the maximum stellar mass are uncertain. Observing the maximum stellar mass can be difficult because we can observe only few stars populating the IMF above $\approx 100M_\odot$. IMFs with high masses of this nature can usually exclusively be found in massive star burst clusters. A survey of the R136 cluster in the Large Magellenic cloud in 1998 found stellar masses up to $155M_\odot$ [34]. However they later explain that this mass limit is due to a statistical limit rather than a physical one [33]. More recent studies of R136 suggest a physical stellar mass limit of $150M_\odot$ [47].

Maximum stellar mass might be limited by its host star cluster mass.

A pre-cluster gas core with a mass M_{core} cannot form stars with masses $m > \epsilon M_{core}$, where $\epsilon = 0.33$ is the star formation efficiency [27]. A recent literature study of clusters for which the cluster mass and the initial mass of the heaviest star can be estimated shows that there appears to be a limit of the maximum stellar mass by the mass of the host cluster [24]. Figure 1.8 shows the dependence of the maximum mass in a cluster versus the mass of the host cluster.

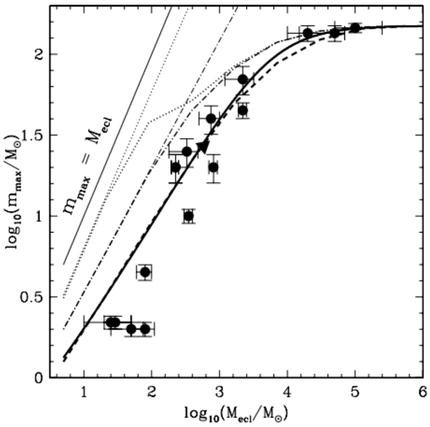

Figure 1.8: The thick solid line follows the dependence of the mass of the most massive star in a cluster versus the host cluster mass. The dots with error bars are observed clusters. The dot dash lines are mass constrained random sampling results with a physical upper mass limit of $150 M_\odot$ (thick line) and $10^6 M_\odot$ (thin line). The thin solid line is the relation when a cluster only contains a single star. This figure is adapted from [24].

The relationship between cluster mass and maximum stellar mass shown in figure 1.8 is important for providing an upper limit on stellar mass. In section 4.2.2 we investigate the relationship between the maximum stellar mass and the host cluster mass found in our simulations.

Chapter 2

Numerical methods to study star formation

Star formation is a complex process and accurate numerical tools are needed to properly incorporate the mass distribution, gravitational collapse, and super-sonic turbulence involved. We use hydrodynamic numerical simulations to properly include these processes to study star formation. Hydrodynamics or fluid dynamics are used to describe the flow of fluids or gases. The fluid dynamics describing molecular gas will of course be governed by gravity which is represented by Newton's second law:

$$\ddot{\vec{r}} = -G \sum_{j \neq i} m_j \frac{\vec{r_i} - \vec{r_j}}{|\vec{r_i} - \vec{r_j}|^3} \tag{2.1}$$

There are many different numerical recipes for hydrodynamics simulations. In this chapter I explain the methods implemented for this paper. I will first draw out basic numerical integrators like the Eularian and the leap frog method. I then introduce some N-body and hydrodynamic techniques. And finally I will describe the code we used for our simulations.

2.1 Nbody

We will be solving Newton's second law of motion, equation 2.1, to describe the motion of gas particles. Since we are dealing with N particle systems, the gravitational force between each particle the system must be calculated. The resulting equations of motion of our system shown in equations 2.2 and 2.3.

$$\dot{v}_i = -\sum \frac{Gm_j}{r_{ij}^3} x_{ij} \tag{2.2}$$

$$\dot{x}_i = v_i \tag{2.3}$$

The indices i & j denote the individual particles. However it becomes very difficult to solve such a system of equations analytically as the number of our particles increases. This is a system of $2 \times N \times Ndim$ equations, where N is the number of particles in our system and $Ndim$ is the number of dimensions. Very few solutions are known for the general N body problem. Current analytic solutions are known only for systems with $N \leq 3$ particles. In the case of $N = 3$ results have been found for special *restricted* cases, where one or more of the masses are infinitesimal. Analytic solutions for systems with more that $N > 3$ particles are very rare and is a current topic in mathematics. In our study we are dealing with systems of $N = 10^6$ particles so we will need to rely numerical methods to solve the equations of motion. In the following section I will draw out two common methods used to solve systems of differential equations numerically.

2.1.1 Integration of ordinary differential equations

One of the most basic numerical approaches is performing a Taylor expansion on the equations of motion, and stepping the equations through time. A common method is the Euler method which uses the 1st order terms of the Taylor expansion.

$$x_i(t + \Delta t) = x_i(t) + \frac{dx_i(t)}{dt}\Delta t + \mathcal{O}(\Delta t^2) \tag{2.4}$$

$$v_i(t + \Delta t) = v_i(t) + \frac{dv_i(t)}{dt}\Delta t + \mathcal{O}(\Delta t^2) \tag{2.5}$$

The Euler method steps equations 2.4 and 2.5 through a time interval Δt. This method of integration is a 1st order integrator, since the numerical precision of this method is 1st order with the numerical error $\mathcal{O}(\Delta t^2)$. This is also an explicit method where it only depends on quantities we know at time t, $x_i(t), \dot{x}_i(t), \ddot{x}_i(t)$. An improvment on the Euler method is the leapfrog method, where the equations are evaluated at $1/2\Delta t$ and is used to step or leap our system through the entire time step Δt. The standard leap frog method is 2nd order accurate as its numerical error is $\mathcal{O}(\Delta t^3)$.

The leapfrog method shown in figure 2.1 calculates the velocity at half the time step and uses that velocity to step the position and acceleration a full time step. After position and acceleration are stepped a full time step the velocity is stepped from half the time set to the full time step, bringing all the equations to the full time step. The method is shown chronologically

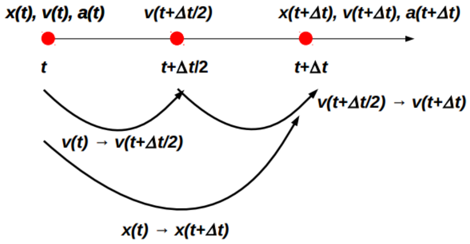

Figure 2.1: Diagram of a 2nd order leapfrog integration method.

with equations 2.6, 2.7, and 2.8, where v_0,$v_{1/2}$ and v_1 is the velocity at the beginning, middle, and end of the time step Δt.

$$v_{1/2} = v_0 + \frac{\Delta t}{2} a_0(x_0) \tag{2.6}$$

$$x_1 = x_0 + \Delta t v_{1/2} \tag{2.7}$$

$$v_{1/2} = v_{1/2} + \frac{\Delta t}{2} a_1(x_1) \tag{2.8}$$

The benefit of a leap frog integrator is that it is time reversible. You can integrate the equations of motion in time n steps and then reverse the same n steps back in time and end up in the exact same place. This means that the leapfrog method is a symplectic integrator. A more precise explanation of symplectic integration is above the scope of this paper, for more reading please refer to [40].

As the number of particles increases, the numerical complexity of the system also increases as $N(N-1)$. If we have a system of $N = 3$ particles we will have to calculate 6 forces. For $N = 4$ we have 12 forces, for $N = 10$ we have 90, for $N = 30$ we have 870 forces. It is easy to see that when we increase the number of particles the numerical complexity of the N-body problem rapidly increases. The number of particles used in this paper is on the order of $N = 10^6$. We will need numerical and computational methods to solve the motions of particles in our molecular clouds efficiently.

2.1.2 Gravitational softening

In N-body simulations particles can sometimes approach each too closely and the force felt between the two can be nonphysical. Since we are integrating through discrete time steps particles can find themselves too close with too big of a step. A way to prevent these spurious events is introducing a softening of the gravitational potential of a particle. The softening is defined as the radius at which the gravitational force is smoothed to a smaller value. In practice, this can be easily illustrated by substituting the force from a point potential

$$F_{ij} = -Gm_i m_j \frac{\vec{r_i} - \vec{r_j}}{|\vec{r_i} - \vec{r_j}|^3} \tag{2.9}$$

to a simple spherical plummer model [39] on small scales [1].

$$F_{ij} = -Gm_i m_j \frac{\vec{r_i} - \vec{r_j}}{(|\vec{r_i} - \vec{r_j}|^2 + \epsilon^2)^{3/2}} \tag{2.10}$$

The softening parameter is ϵ in equation 2.10. The value is a sort of a rule of thumb of each simulation, it can be taken as the average distance between particles. For astrophysical systems we can estimate it using the virial radius R_{vir} and the number of particles in a simulation N.

$$\epsilon = (\frac{4\pi R_{vir}^3}{3})^{1/3} N^{-1/3} \tag{2.11}$$

2.1.3 Barnes-Hut Tree Method

Direct N-body integration calculates every single force between all of the particles in a simulation. Systems that require direct N-body methods are systems that have strong gravitational interactions between single particles. Interactions between single particles can influence the overall evolution of the system. The numerical integration in direct N-body methods requires $\approx N^2/2$ calculations to evaluate the potential energy generated by all particle pairs. This proves to be very computationally expensive.

The numerical integration of gas clouds does not need to be studied with direct N-body as the gravitational interaction between single particles do not change the evolution of the entire cloud. The simulation of a gas cloud evolves smoothly and can be treated as a fluid. We can rely on indirect N-body methods in order to solve high N problems.

The Barnes-hut Tree method is an approximation algorithm used to reduce the numerical complexity of a N-body system to the order of $\mathcal{O}(N \log N)$ rather than that of the direct method, $\mathcal{O}(N^2)$. We do not need to calculate each individual force on each particle. The cumulative force of a group of particles can be estimated if the group of particles is sufficiently far. A group of particles that is far enough can be estimated as a single particle, with the location at the center of mass, and the total mass of the group as the mass.

The Barnes-Hut tree method recursively divides up the simulation space into cells. Each cell is divided into further cells, which are further divided

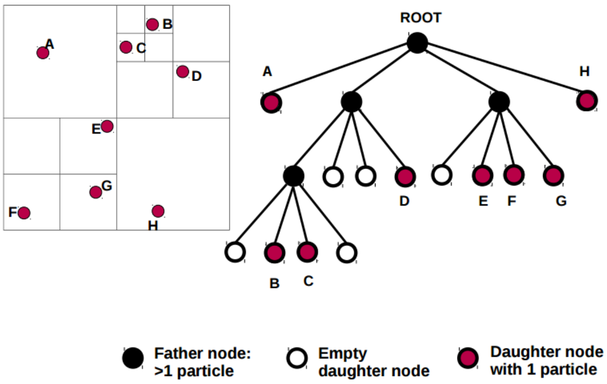

Figure 2.2: Diagram of a Barnes-Hut tree method showing the simulation space divided into cells. Here the father node has more than one particle and is further divided into daughter cells until it contains one or no particles.

up until each cell has a single or no particle inside of it. This is called a tree method because the largest cell can be thought of as the main root of the tree, where the sub cells are the branches and the smallest sub cells containing the particles are the leaves. A diagram of this method is shown in figure 2.2.

$$\theta = \frac{s}{d} \tag{2.12}$$

A quantity called the opening angle, equation 2.12, determines when a particle will be treated as a single particle or when it will be treated with a group of particles (in other words how far a particle needs to be in order to avoid direct calculation). The opening angle θ is dependent on s the width of the region represented by the considered cell and d the distance between the particle and the center of mass of the cell. The opening angle is defined before running the simulation. $\theta = 0.5$ is common in practice. When $\theta = 0$ the Tree algorithm will degenerate into the direct N-body method.

In the figure 2.2 we see that particles close by each other will have their direct mutual gravity calculated, particles E and F for example. Where as particles far away from each other will have their mutual gravity approximated by using the total mass and center of mass of a cell. As an example the force felt by particle D by particles E, F, and G. Particles E, F, and G will have their masses summed and the location of their summed mass will be at the center of mass of E, F, and G.

2.2 Hydrodynamics

When trying to simulate the motions of gas particles we are not only governed by Newton's equation (equation 2.1). We are also governed by fluid mechanics which are given by Euler's equations 2.13, 2.14, 2.15, and 2.16.

$$\frac{\partial \rho}{\partial t} + \nabla \cdot (\rho \vec{u}) = 0 \tag{2.13}$$

$$\frac{\partial \rho \vec{u}}{\partial t} + \nabla \cdot (\vec{u} \times (\rho \vec{u})) + \nabla p = 0 \tag{2.14}$$

$$\frac{\partial E}{\partial t} + \nabla \cdot (\vec{u}(E + p)) = 0 \tag{2.15}$$

$$E = \rho(U + \frac{\vec{u}^2}{2}) \tag{2.16}$$

With the mass density ρ, fluid velocity $\vec{u}$, thermal pressure p, total volume energy density E, and internal energy U. There are in general two methods used to solve these fluid equations numerically namely Eularian and Lagrangian. A popular method used in the Eularian scheme is called Adaptive Mesh Refinement (AMR), which uses a mesh grid in Cartesian space to resolve the physics of a fluid to some specified scale. A popular method in the Lagrangian scheme is smoothed particle hydrodynamics (SPH), where the coordinates of the simulation move with the fluid. Both methods are currently used in astrophysical simulations.

2.2.1 Smoothed particle hydrodynamics (SPH)

Smoothed particle hydrodynamics is a computational method used to simulate fluids by dividing up the fluid into discrete particles. The coordinates of the simulation move with the fluid (Lagrangian) and the resolution of the simulation can be adjusted to the physical properties of the fluid. The physical elements of the fluid are smoothed over the discrete particles using a smoothing kernel. The discrete particles have a physical radius called the smoothing length h, and over this length the physical properties of the fluid are smoothed. The smoothing length is defined as the distance at which a simulation particle has N neighbors, which is typically chosen to be $N = 32$ or $N = 64$. This is similar to the gravitational softening length, but in this case the gas properties (pressure, density, temperature) are smoothed. The contributions of each of particle to a physical quantity A will be weighted according to their distance r to another particle and their density ρ:

$$\vec{A}(\vec{r}) = \sum_i m_i \frac{\vec{A}_i}{\rho_i} \vec{W}(|\vec{r} - \vec{r_i}|, h) \tag{2.17}$$

As an example we can express the density of particle i as

$$\rho_i = \rho(\vec{r_i}) = \sum_i m_i \frac{\rho_i}{\rho_i} \vec{W}(|\vec{r} - \vec{r_i}|, h)\rho_i = \sum_i m_i \vec{W}(|\vec{r} - \vec{r_i}|, h) \tag{2.18}$$

It is important to choose the smoothing length close to the gravitational softening length. If the smoothing length is greater than the softening length ($h > \epsilon$) then the gravity is stronger than the pressure of the gas and we will have spurious collapse. Also if the smoothing length is less than the softening length $h < \epsilon$ gas pressure will dominate and we will have spurious expansion. It is important for the correct resolution of our simulations to have $h \approx \epsilon$ [2].

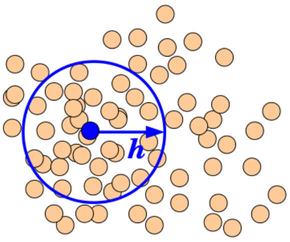

Figure 2.3: Diagram showing the softening length over N neighbors. The properties of the gas will be smoothed over the discrete simulation particles, light pink circles, that fall within the smoothing length h.

A diagram of the smoothing length is shown in figure 2.3. The smoothing kernel must be a function that is normalized to one and easy to interpolate at high precision. It must also be a function that is spherically symmetric so it will conserve angular momentum in the simulation.

The benefit of SPH is that is relatively simple compared to AMR methods. You are able to choose the gravitational softening length, smoothing length, and the number of particles in your simulation to set the resolution of the simulation. The SPH method refines the resolution automatically as the simulation progresses through time. If a region of gas collapses in on itself the SPH method will adjust the density in the region automatically as needed. One drawback of the SPH method is that it does not resolve strong shocks.

2.3 ChaNga

When we deal with systems under the influence of gravity we have to calculate the force between every particle in the simulation. As the number of particles exceeds 10^5 this becomes too computationally expensive to calculate with just a single processor. We require parallel computational methods since the systems we are interested in solving have $\approx 10^6$ particles. Most basically when we use multiple processors the particles N are distributed between the number of processors p. The simplest way to split the particles up is N/p, but there exists more complicated algorithms. Each processor calculates a portion of the forces between particles at each time step and the information from all processors at each time step is collected and the system is stepped forward.

The code used in this paper is ChaNga (Charm N-body GrAvity solver) which includes most of the numerical and computational methods mentioned above [35]. It is a SPH parallelized code written in the CHARM++ run time system, with good run time work-load balance where integration and particles are well distributed between processors. It uses a Barnes-Hut tree algorithm where each leaf can contain more than a single particle. It uses a cubic spline for gravitational softening.

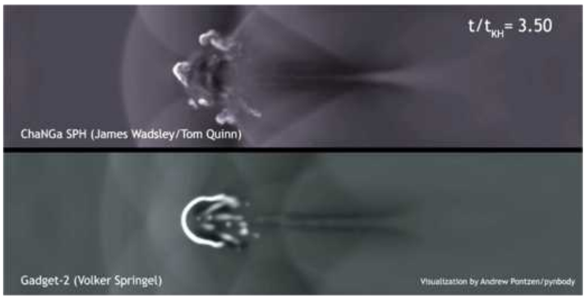

Figure 2.4: Example of gas physics simulation using ChaNGa (top panel) compared to another SPH hydrodynamic code GADGET-2 (bottom panel). The simulation is of a high dense region of gas under the influence of an external wind. The ChaNGa code shows better treatment of instabilities rapidly mixing the high density region with the surrounding medium. Time is shown in units of the Kelvin-Helmholz growth time.

In figure 2.4 we see an example of the capabilities of handling gas physics with ChaNGa. Here is a two panel image comparing ChaNGa to older SPH code GADGET-2 [44] simulating a high density cloud in pressure equilibrium in a wind. Figure 2.4 shows how artificial surface tension and instabilities rapidly mix the high density region with the surrounding medium. Gadget-

2 in the lower panel shows how poor handling of contact instabilities will preserve the high density region. ChaNGa gives similar results to alternative hydrodynamic codes like ENZO, which uses Adaptive Mesh refinement [9].

Chapter 3

SPH simulation of a single molecular cloud collapse

In this chapter I test the performance of my new star identification algorithm which identifies newly formed stars from our gas simulations. Simulations cannot follow the collapse of gas till the formation of a new star, because the involved density range is computationally prohibited. Thus, sink particles are created to replace a clump of collapsing gas particles. These can be very useful for modeling forming stars within a hydrodynamic simulation if the proper recipe is used. In section 3.1 I describe my new sink identifying algorithm and how it can be used to create sink particles. In section 3.2 I simulated the collapse of a single molecular cloud. Finally in section 3.3 I test the my sink finding algorithm by producing a mass function close to the Salpeter IMF.

3.1 Sink identifying algorithm

Tracking star formation within our simulations was done following recipes of [20] and [15]. Star candidates need to satisfy 4 criteria to be classified as a formed star. In our simulations we did not implement a sink creating algorithm, rather we ran our simulations until significant clumpiness was achieved and analyzed the stellar candidates postmortem. This was done to keep from spurious sink creation during our simulations. An example of a spurious sink would be identified by a density criterion while not having a diverging velocity field. The sink may be falsely created too early. The region maybe dense enough, but it could later in the simulation be destroyed by a transient velocity field. Our final identified stars will satisfy density criterion, non-overlapping criterion, velocity divergence criterion, and total energy criterion. If a candidate satisfies all four of these criteria, in order, we identify it as a formed star.

1: Density The first criterion is the density criterion. A candidate is identified first if its density exceeds our threshold density. This threshold density is chosen as $\rho_{sink} = 10^{-12} gcm^{-3}$ as this is well into the Kelvin-Helmholtz contraction phase.

2: Overlap The second criterion is that sinks do not overlap each other when they are created.

$$|r_i - r_{s'}| \leq R_s + R_{s'} \tag{3.1}$$

On the left hand side of equation 3.1 we have the modulus of the distance between the centers of the two particles. On the right hand side we have the physical radius $R_s = X_{sink} h_i$ of our candidate star particle and $R_{s'}$ the physical radius of an existing candidate star particle. The physical radius is given by its smoothing length h_i, multiplied by a user provided parameter $X_{sink} = 2.0$ following current sink implementation recipes [20]. In the case when multiple SPH particles exist within the physical radii of a candidate particle we chose the particle which was most dense. In the rare occasion that particles have the same density we chose the one that is closest to the center of mass of the local clump.

3: Velocity Divergence Once the first and second criterion are satisfied we check whether the divergence of the velocity field at our particle i is negative i.e.

$$(\nabla \cdot v)_i < 0 \tag{3.2}$$

The divergence was calculated over a selection radius centered on the particle i. This selection radius was taken as 0.015 times our initial softening length. This was found by taking multiple different radii each with a different factor of our softening length and seeing which radius gave us the best fit to the Salpeter initial mass function. This selection radius was also used in our energy criterion.

4: Total Energy The final criterion a star candidate particle has to obey is whether its energy is negative (i.e. where the gas clump is bound). This was done by calculating the total energy, consisting of its potential energy $E_{grav} = \frac{G \cdot m_i \cdot m_j}{r_{ij}}$ and the kinetic energy, $E_{kin} = \frac{1}{2} m_i v_i^2$. Each of the energies were calculated in the center of mass frame in order to eliminate contributions due to global motions of the cloud.

Table 3.1: Star creation criteria

Creation Criterion	Equation
Density	$\rho_i > \rho_{sink}$
Overlap	$\|r_i - r_{s'}\| \leq R_s + R_{s'}$
Velocity Divergence	$(\nabla \cdot v)_i < 0$
Energy Bound	$E_{grav} + E_{kin} < 0$

It is important to note that we take the local velocity divergence because we are interested local convergences rather than global convergences. If we calculate the global divergence we might ignore local convergences and miss star formation sites. Globally our entire cloud is marginally bound in energy by construction. After a candidate has successfully fulfilled all four criterion we classify the candidate as a formed star.

3.2 Initial conditions and cloud collapse

To test the sinkfinder algorithm, I simulated the collapse of a single turbulence-supported molecular cloud with an initial radius and mass of $R_{cloud} = 10$ pc and $M_{cloud} = 4.3 \times 10^4 M_\odot$. The cloud has an initial uniform density of $\rho_0 = 6.94 \times 10^{-22}$ gcm^{-3} and is given a molecular wight of $\mu = 2.46$. The initial temperature of the cloud is 10K.

Table 3.2: Single cloud conditions

Cloud	$N/10^5$	r_0 [pc]	v_0 [kms^{-1}]	turbulence seed	T [K]	μ
A	1.0	$(0, 0, 0)$	$(0, 0, 0)$	72299	10.0	2.46

Interstellar turbulence in the cloud was generated from a velocity field with an imposed power spectrum of $P(k)$ with the power varying as k^{-4}. The velocity field was created by first generating a grid of velocities using a divergence free Gaussian field, which was randomly distributed using a Monte Carlo method. The Monte Carlo method was seeded from an random integer which was given by personal choice. The final velocities were interpolated from this grid onto the gas particles. The resulting velocity field follows a velocity dispersion σ, which falls off as $l^{1/2}$. This was chosen to agree with the Larson's scaling relations which was covered in section 1.4.3. The velocity field is supersonic. The gas cloud is also marginally bound i.e. initially $E_{kin} \simeq E_{grav}$.

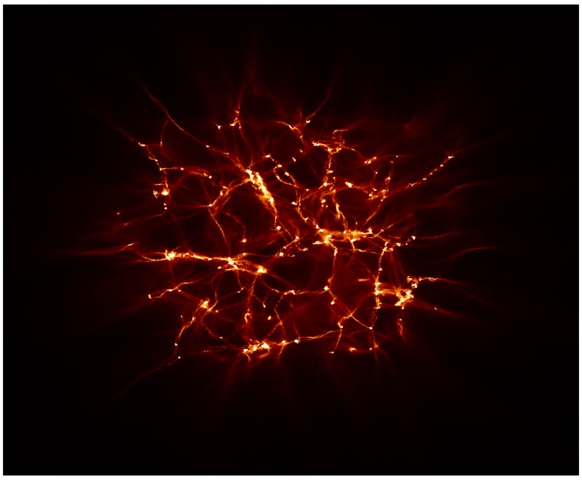

Figure 3.1: Snapshot of the single molecular cloud which has collapsed under its own gravity. Here the extremely bright regions on the filaments are regions where the gas of the cloud is dense enough to form stars and star clusters. The snap shot is 1.5 pc to a side. The bright regions have a density of $\rho \approx 10^{-12}\mathrm{gcm}^{-3}$ and will be considered in our criteria for forming stars. This image was produced using SPH viewer [4] where the density of each simulation particle was smoothed over 64 of its neighbors. The smoothing length of each particle was included to produce this image.

The snapshot of the collapsed single cloud shown in figure 3.1 shows many dense clumps along with filament structures. The clumps are regions where the gas cloud has collapsed enough to start forming stars. The filament structures are produced by the initial turbulent velocity field and by the infalling gas. This dense area is located in the central region of the simulated molecular cloud. The initial cloud had a radius of 10pc, where the filaments and the denser star forming regions occur on scales of $\approx$ 1 pc after the cloud has significantly collapsed in on itself.

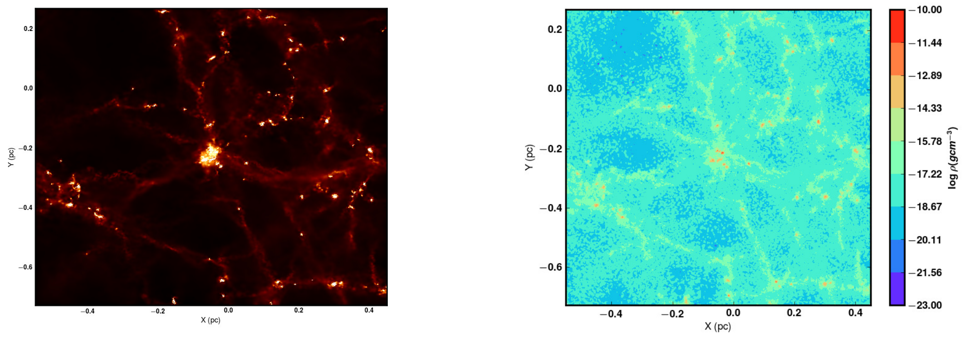

Figure 3.2: The central region of a collapsed single molecular cloud. The regions shown in each panel are 1pc to a side. The right panel is a contour map illustrating the density of the clump and filament regions. In the most dense clumps the density exceeds densities of 10^{-12}gcm^{-3}.

In figure 3.2 we focus on a region close to the center of mass of the cloud. In the left panel we see dense star forming regions located on a backdrop of multiple connecting filaments. The right panel contour map illustrates the density of each of the structures.

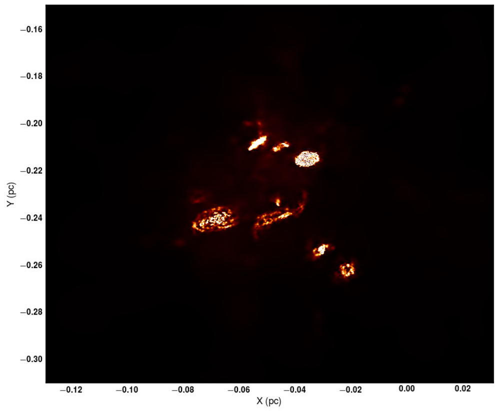

Figure 3.3: The densest regions (approximately 10^{-3} pc) are areas in which the gas is collapsed to form stars. The image illustrates the location of many stellar systems. This snapshot is 0.8pc to a side.

Figure 3.3 is an even closer look into the different regions of high density. The size of each dense clump is approximately 10^{-3}pc which is close to the spatial resolution of our simulations. Remember we are using a softening length of 0.5×10^{-5}kpc. The current understood size of proto-planetary disks is approximately 100AU [48] which corresponds to a length of $\approx 4.84\times10^{-4}$pc. In figure 3.3 we are able to see the neighborhood of individual stars or star systems being formed. We stress that magnetic fields were not included in our simulations. Thus, we cannot statistically reproduce the evolution of protoplanetary disks.

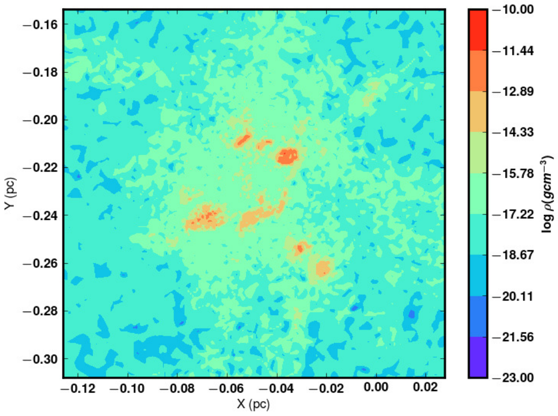

Figure 3.4: A contour plot of the region shown in figure 3.3 colors the most dense and compact regions in the simulation. Each compact region which will likely form single to multiple stars exceeds densities of 10^{-12}gcm^{-3}.

In figure 3.4 we see the zoomed in region of figure 3.3 illustrated using a contour map colored off of density. Note that in section 3.1 the initial criteria we use to identify formed stars in our simulations is that a simulation particle's density must be greater than 10^{-12}gcm^{-3}. Figure 3.4 shows that there are many regions exceeding this threshold.

3.3 Testing the sinkfinder

Our simulation was run until the cloud exhibited sufficient clumpiness by eye, and the time steps of our simulation slowed down significantly due to the clumpiness. We checked snapshots of the simulations for formed stars. We also calculated at each snapshot the amount of cloud mass that satisfied the four criteria, because we will stop the simulation when 10% of the cloud mass has converted into stars. We expect star formation to happen around $t \approx 2.3 \times 10^6$yr because the dynamical time of our cloud is $t_{dyn} = 2.5$ Myr.

The number of stars that satisfy the four criteria is plotted in figure 3.5. The number of stars that satisfy the density criterion is many times greater than the number of stars that satisfy the other three criteria. The overlap

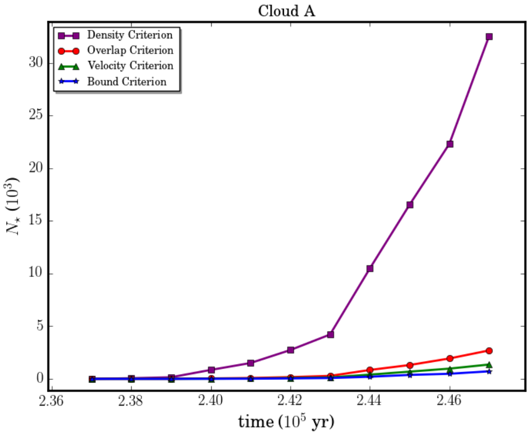

Figure 3.5: Number of star particles found by our 4 criteria as a function of time, in cloud A. This is the main test of the algorithm

criterion significantly reduces the candidacy of stellar particles because many of the particles which satisfy the density criterion lie within the interaction radius of another dense particle.

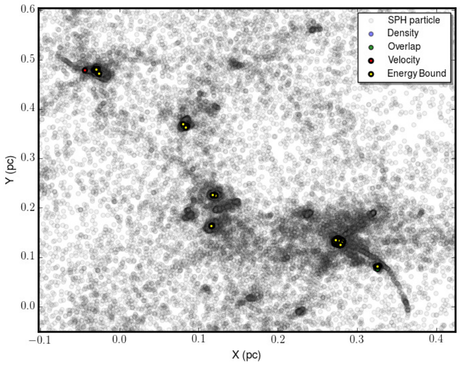

Figure 3.6: A wide view snapshot of a dense star forming region in cloud A. The particles are colored off of the criteria they satisfy; density criterion faded (blue), overlap criterion (green), velocity divergence criterion (red), and energy criterion (yellow).

Figure 3.6 is a zoom in on multiple dense regions in the cloud. We are able to see approximately six locations where the simulated particles satisfy our star identification criterion. We also see a large spider leg like structure in the location of $X \approx 0.35$ pc & $Y \approx 0.05$ pc. This structure is likely part of a larger filament which is caused by super sonic turbulence. At the end of this leg structure we find a very dense region where multiple particles are satisfying our star identification criteria.

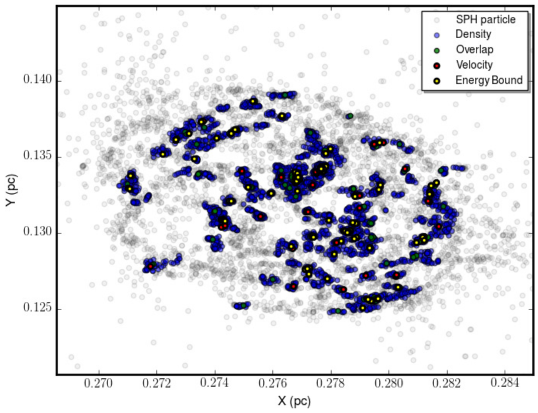

Figure 3.7: A snapshot of individual clusters of particles in part of a larger dense complex in the cloud. The particles are colored off of the criteria they satisfy; density criterion (blue), overlap criterion (green), velocity divergence criterion (red), and energy criterion (yellow).

Well over hundreds of particles in this region, shown in figure 3.7, satisfy our density threshold criteria, colored in blue. In green we have stars that satisfy overlap criteria. In red particles that satisfy velocity divergence criteria, meaning that the velocity field around that particle is converging. And finally we have our final identified stars in yellow, that is candidates which satisfy even the energy criterion. We can see that even in this snapshot exists tight groups of stars.

Finally we can look at one of these clusters in detail shown in figure 3.8 which illustrates multiple stars in a single cluster. Here around 20 stars exist in single and binary systems. Note that the particles shown in Figures 3.6, 3.7, and 3.8 do not illustrate the physical picture of what is happening well in the simulation snapshot. It is important to refer to figures 3.1 and 4.1 for a more complete illustration since they use each particle's mass and individual smoothing length to convey density. The snapshots in this section are used merely to show location of candidates which satisfy the stellar candidate criteria.

3.3.1 Reproducing the initial mass function

In order to test the accuracy of the star finding criteria we attempt to reproduce an IMF from the identified stars. We choose to compare the IMFs

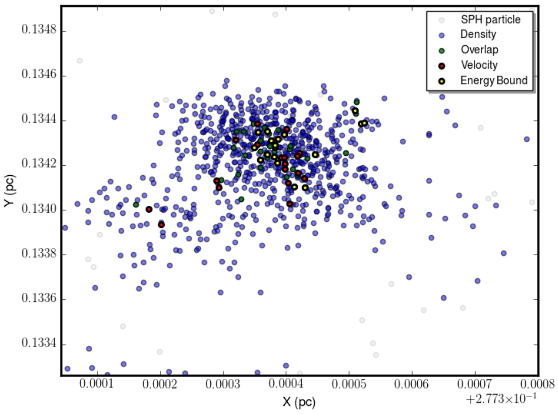

Figure 3.8: Individual stars as a part of a larger new star cluster. The particles are colored off of the criteria they satisfy; density criterion (blue), overlap criterion (green), velocity divergence criterion (red), and energy criterion (yellow).

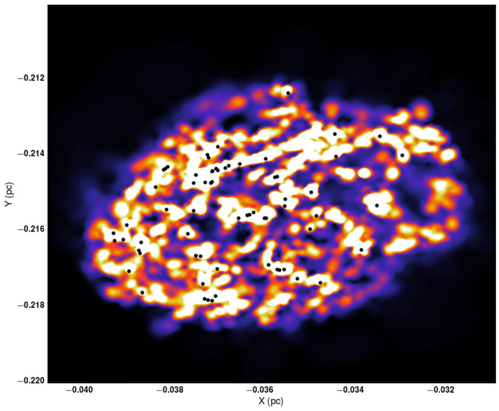

Figure 3.9: Stars found from the four criteria plotted on a zoomed in region of the cloud. This region appears to have a flattened disc due to the conservation of angular momentum added by in falling gas.

produced by our simulations to the mass spectrum predicted by the Salpeter IMF. Again the Salpeter IMF is a single power law with a slope of $m^{-2.35}$. The mass of the final star is determined by the radius at which calculate the 3rd and 4th criteria, the velocity convergence and the energy criteria. The total mass is the amount of simulation particles that will accreate to our star particle. The final mass of the star will be made up of all the simulation particles which will collapse, flow onto, and are bound to the star particle.

We first populate a mass spectrum from a single turbulence supported cloud collapsing in on itself, the same cloud used in section 3.2. The cloud was evolved for 0.247 Myr. At this time $\approx$ 10% of the cloud mass was converted into stars. We find that in the order of magnitude range of 10^{-2} of our softening length we start to produce a reasonable mass spectrum. The radius that we used to produce the mass spectrum is 0.015 times our softening length. The softening length is a good choice because it is the scale on which the pressure and the gravitation of our simulation is resolved.

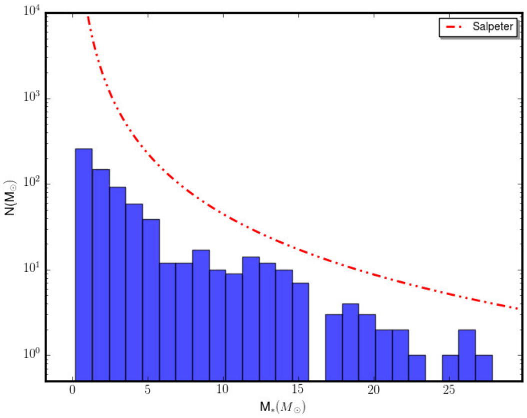

Figure 3.10: Shown here is an IMF, in semi log space, generated from the collapse of a single cloud. Stellar mass M_* on the x-axis and the logarithm of stars per mass bin $N(M_*)$ on the y-axis. We compare our result to the Salpeter IMF $dN/dm \propto m^{-2.35}$, dashed red line.

In figure 3.10 is the mass spectrum in linear-log space, with the logarithm of number of stars in each linear mass bin. We expect to see much more stars populate the lower mass range around 0 to $5M_\odot$. And we also expect that the number of stars to decrease with increasing mass. The mass spectrum produced from cloud A seems to follow this trend while being slightly insufficient in masses below $5M_\odot$.

We are able to see how the mass spectrum from cloud A matches the Salpeter in the higher mass range. Stars with masses $\geq 20M_\odot$ follow the slope of $m^{-2.35}$ pretty well. However the lower mass of the spectrum still is insufficient. This seems to be because of the limit of the mass resolution in our simulations. Since the cloud is $4.3 \times 10^4 M_\odot$ and composed of $N_{cloudA} = 10^6$ SPH particles the mass of each individual particle is $\approx 0.04M_\odot$.

3.3.2 Producing IMF through other radii

In order to test the accuracy of our choice in radius we produce multiple mass spectra by taking multiple radii to calculate the divergence and energy criteria. We take a larger 0.02 and a smaller 0.01 radius than what was used to produce figure 3.10, which is 0.015 times the softening length.

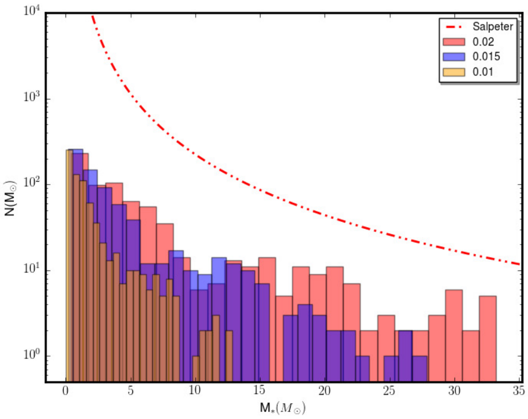

Figure 3.11: The IMF produced in semi log space. Logarithm of the number of stars on the y-axis per mass bin (solar masses) on the x-axis. Each colored histogram corresponds to a different radius taken to define stellar mass. Each is a factor of the gravitational softening length (ϵ), red (0.02), blue (0.015), and yellow (0.01).

The larger radius produces a mass spectrum which is over abundant in the higher mass range. While the 0.01 softening length radius produces less in the higher mass range. All three radii are compared to each other in semi log space in figure 3.11. The difference in the higher mass range is more evident in the log log space, figure 3.12.

It seems that the choice $0.015 \times \epsilon$ is the best at the current resolution. We are limited in populating the lower mass range due to the mass resolution of our simulations.

High resolution check

We ran another single cloud with the same initial conditions used in section 3 but in this case we increased the mass resolution by increasing the number of particles the simulation. Previously our single cloud collapse consisted of $N = 10^6$ SPH particles. Now we have increase the number of particles by a factor of 5 which will increase the mass resolution. With a total number of

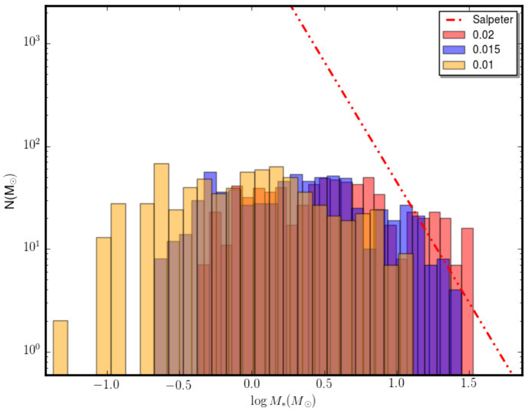

Figure 3.12: The mass functions in log log space. Logarithm of the number of stars on the y-axis versus the logarithm of solar masses on the x-axis. Each colored histogram corresponds to the different radii taken to define stellar mass. Each is a factor of the gravitational softening length (ϵ), red (0.02), blue (0.015), and yellow (0.01). The Salpeter mass spectrum is shown with the dashed red line.

particles of $N = 10^6$ the mass of each SPH particle is $\approx 0.04M_\odot$. When we increased the number of particles to $N = 5 \times 10^6$ the mass of each particle is $\approx 0.0086M_\odot$. We observe the impact of this resolution with the IMFs produced in figures 3.13 and 3.14. We see in both semi log and log spaces that the population of stars formed is much more on the lower mass end of the spectrum when compared to the $N = 10^6$ case. We also see that the we are producing less stars in the high mass range. Again, we see that different radii influence the spectrum of masses produced.

It is a current problem in numerical studies of star formation to be able to produce the full initial mass function. We use the high resolution case as a confirmation that the star identifying algorithm discussed in section 3.1 is working. As we increase the mass resolution of our simulations we start to produce lower mass stars and begin to lack in high mass stars. A comparison of the $N = 10^6$ mass spectrum with the $N = 5 \times 10^6$ high resolution mass spectrum is shown in figure 3.15.

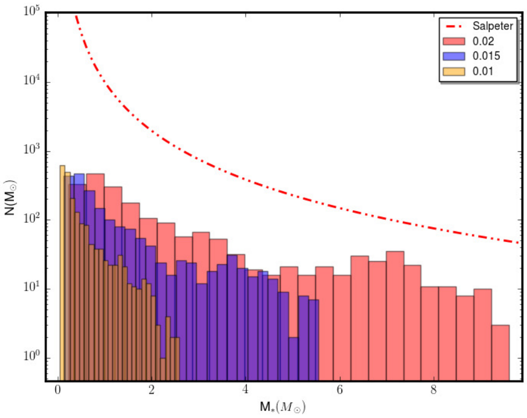

Figure 3.13: The high resolution run of the single cloud collapse. On the y-axis is the logarithm of the number of stars per mass bin (solar masses) on the x-axis. Each colored histogram corresponds to a different radius taken to define stellar mass. Each is a factor of the gravitational softening length (ϵ), red (0.02), blue (0.015), and yellow (0.01).

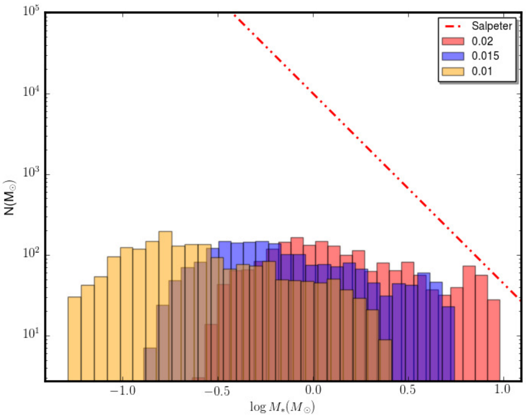

Figure 3.14: The mass functions in log log space of the high resolution run of the single cloud collapse. Logarithm of the number of stars on the y-axis versus the logarithm of solar masses on the x-axis. Each colored histogram corresponds to the different radii taken to define stellar mass. Each is a factor of the gravitational softening length (ϵ), red (0.02), blue (0.015), and yellow (0.01).

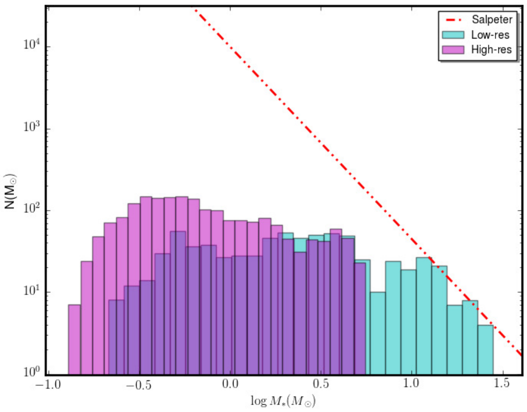

Figure 3.15: The mass function in log log space of the high resolution run ($N = 5 \times 10^6$), shown in magenta, compared with the normal resolution run ($N = 10^6$), shown in cyan. Logarithm of the number of stars on the y-axis versus the logarithm of solar masses on the x-axis. The radius taken to define the stellar mass is a factor of 0.015 of the gravitational softening length ϵ in both cases.

Chapter 4

Star formation from molecular cloud collisions

In this chapter we investigate the star formation induced from two molecular clouds colliding at different velocities. We are aiming to see how the velocity of the collision of the two clouds will affect star formation, when stars form during the collision, and how that depends on the velocity of the two clouds. We set up six simulations of the colliding clouds. Each simulation is given initial velocities of 0, 2, 4, 6, 8 and 10 $\mathrm{km\,s^{-1}}$. The simulations are run until 10% of the total mass of each collision is converted into stars. We track the time stars begin to form in each collision, until the end of the simulation. We produce density contour maps of each collision to see where the stars are forming. And we check that the mass spectrum of the formed stars follows the Salpeter IMF in each simulation.

4.1 Initial conditions

First our two clouds, named A & B, consisting of $N_A = N_B = 10^6$ particles each were simulated independently in absence of any collision. A detailed analysis of these single clouds can be found in chapter 3. This was done as a baseline to see how many stars were formed out of the two respective clouds if they were to collapse by them selves. Our clouds initially have a radius and mass $R_{cloud} = 10$ pc and $M_{cloud} = 4.3 \times 10^4 M_\odot$. Which gives us an overall density of $\rho_0 = 6.94 \times 10^{-22}$ $\mathrm{gcm^{-3}}$. The initial temperature of both clouds are $T = 10K$ and of a molecular weight of $\mu = 2.46$. All of our simulations are nearly isothermal with a $\gamma = 1.001$. We give a gravitational softening length of 0.5×10^{-5} kpc to the SPH gas particles. Both clouds are supported by supersonic turbulence and marginally bound, described in detail in section 1.4.3. To reproduce interstellar turbulence within the cloud, the velocity field of each cloud was generated from a grid using a divergence-free Gaussian random field with an imposed power spectrum $P(k)$, varying as k^4. Each Gaussian random field was generated through Monte-Carlo method that was seeded with an integer of our choosing.

Table 4.1: Initial Cloud conditions

Cloud	$N/10^6$	(x_0, y_0, z_0) [pc]	turbulence seed	T [K]	μ
A	1.0	$(0, 0, 0)$	72299	10.0	2.46
B	1.0	$(22, 0, 0)$	34213	10.0	2.46

In table 4.1 we see the initial conditions of each cloud. Here cloud A and cloud B have the same radius, mass, molecular weight, temperature, but they differ in the initial seed from which the turbulent velocity field is populated. The seed is a personal choice and only serves as the seed to build the velocity distribution via Monte-Carlo method. The clouds will have the same overall physical attributes but they will differ in the spatial structure of their supersonic turbulence fields. Both cloud A and B are kept the same in every collision.

In each collision we set cloud A at rest at the origin, i.e. $(x_0, y_0, z_0) = (0, 0, 0)$ pc and $(v_{x0}, v_{y0}, v_{z0}) = (0, 0, 0)$ kms^{-1}. We collide this cloud with cloud B, which is placed at a position just outside the radius of cloud A, so that the clouds are close but not touching. Since the radius of each cloud is 10 pc we set cloud B at $(x_0, y_0, z_0) = (22.0, 0, 0)$ pc with an initial velocity $(v_{x0}, v_{y0}, v_{z0}) = (v_0, 0, 0)$ kms^{-1}. We vary v_0 in each of our collisions, see table 4.2. This range of velocities was selected to reflect typical relative velocities of collisions between molecular clouds in the disk of a barred galaxy [16].

Table 4.2: Initial conditions

Run	$N/10^6$	Velocity of cloud B v_{x0} $[km/s]$	E.O.S.
1	2.0	-2.0	Isothermal
2	2.0	-4.0	Isothermal
3	2.0	-6.0	Isothermal
4	2.0	-8.0	Isothermal
5	2.0	-10.0	Isothermal

4.2 The collisions

Star formation in each collision usually begins after the clouds have significantly collided with each other. We cannot say for sure when the centers collide, since the clouds begin to deform due to the gravitational influence each cloud has on its partner before the centers reach each other. In the collision at 2 kms^{-1} we observe that star formation occurs much earlier than the collision between the two centers. In contrast, in the 10 kms^{-1} case the clouds significantly collide before star formation takes place. In general we find that star formation is induced earlier as collision velocity increases, as shown in figure 4.3.

A good schematic view of the 10 kms^{-1} collision is shown in the four panel figure 4.1. This is the highest velocity collision and shows that each cloud hasn't had enough time to collapse enough before the colliding. In this case, the collision induces the star formation. The collisions 4, 6, 8 and 10 km s^{-1} follow this trend while in the 0 and 2 kms^{-1} cases the clouds deform significantly as they fall into each other.

The star identifying algorithm shows no significant change through each collision. The four identification criteria are satisfied generally the same at each velocity, as shown in figure 4.2.

We can compare the star formation vs time for each collision, as shown in figure 4.3. Star formation begins and finishes earlier as the velocity increases. Detailed information regarding star formation beginning and ending times with respect to each collision is displayed in table 4.3.

Table 4.3: Star Formation Times

Run	v_{x0} [km s^{-1}]	Star formation begins [Myr]	Star formation ends [Myr]
1	-2.0	0.24	0.25
2	-4.0	0.20	0.21
3	-6.0	0.18	0.20
4	-8.0	0.18	0.18
5	-10.0	0.17	0.18

It is important to note that we do not mean that the total time it takes to form stars is shorter depending on the velocity, as it is roughly the same time for each cloud from beginning to end of star formation. We mean that the 10 km s^{-1} simulation will be done forming stars well before the 6 km s^{-1} cloud will begin. And well before the 0, 2 and 4 km s^{-1} clouds will begin their star formation.

We choose not to show a snapshot or a contour map of the 0 km s^{-1} collision since the same information can be shown with the 2 km s^{-1} collision.

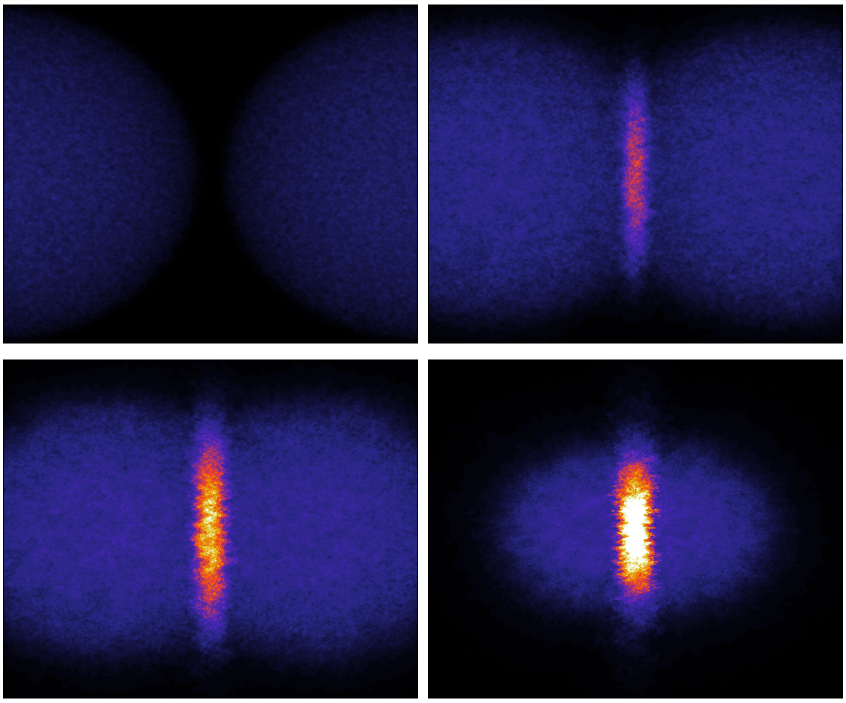

Figure 4.1: Snapshot in the center-of-mass frame of a head-on collision at 10 $\mathrm{km\,s^{-1}}$. Here we highlight the low density environments with $\rho \approx 10^{-20}$ $\mathrm{gcm^{-3}}$ to show the shape of the clouds. The frames are at 0.1, 0.8, 1.2 and 1.84 Myr. The final frame is when the simulation was stopped, i.e. 10% of the cloud mass formed stars.

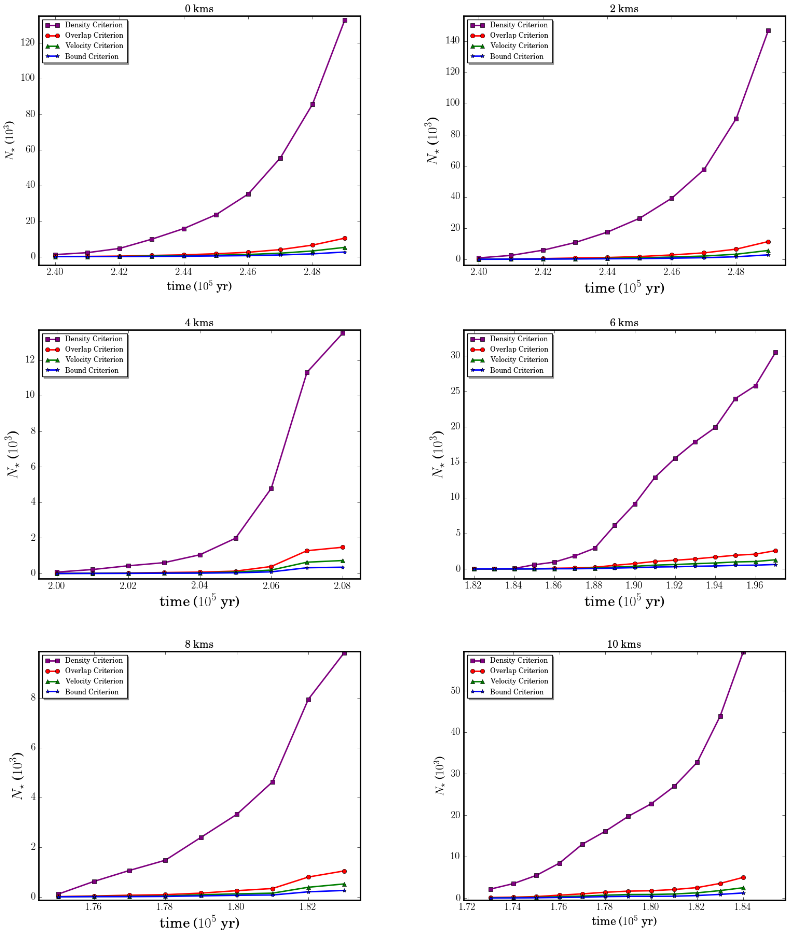

Figure 4.2: The four panels show our stellar candidate identification criteria across increasing collision speeds, with initial velocities of 2, 4, 6 and 8 km/s. If only the density criterion (Purple Boxes) is applied, we find many more stars than by applying also the other criteria, as each system evolves with time.

In both cases, the clouds collapse onto themselves and form stars significantly before colliding.

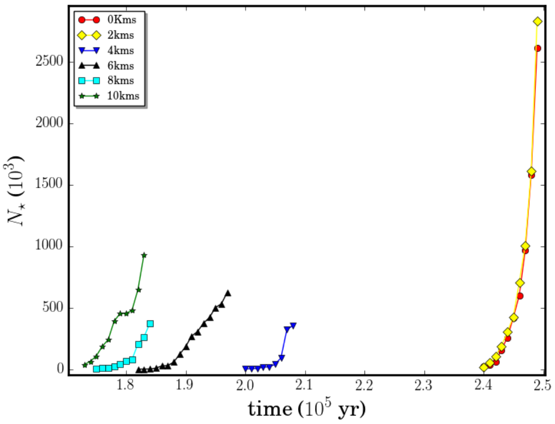

Figure 4.3: Number of formed stars at increasing collision speeds. Star formation begins earlier as the speed of the incoming cloud is increased. Each simulation is stopped when 10% of the cloud mass formed stars. At low velocities, 0 and 2 km s^{-1}, the total number of stars formed is greater and formed much later than at higher velocities.

A snapshot of the 2 km s^{-1} collision is shown in figure 4.4. The left panel shows the total zoomed out simulation as viewed perpendicular from the collision. We observe significant star formation in the center of each cloud along with a large filament structure falling from each cloud towards the center of mass of the system. Stars form along this global filament preferentially closer to the centers of each cloud. Each cloud still has most of its original spherical shape when star formation begins, and has its own filament complex due to the in fall of gas with the initial super sonic turbulence.

We can look in detail of the density of these regions and where the stars are forming in the clouds by producing contour maps. Shown in figure 4.5 are four contour maps each highlighting a different scale and region in the 2 km s^{-1} collision. Since this collision did not result in a significant collision plan we focused on showing all contour maps from the side view of the collision.

As the velocity increases we begin to see piling up of gas with densities exceeding $\rho > 10^{-19.5}$ gcm^{-3} along the plane of collision (Y-Z plane). This plane grows along the X-axis and in density as collision speed increases. The 4 km s^{-1} plane has a thickness of 0.5 pc spanning from $X = -0.1$ pc to $X = 0.4$ parsec. The 6 km s^{-1} plane grows to a thickness of 1 pc which spans

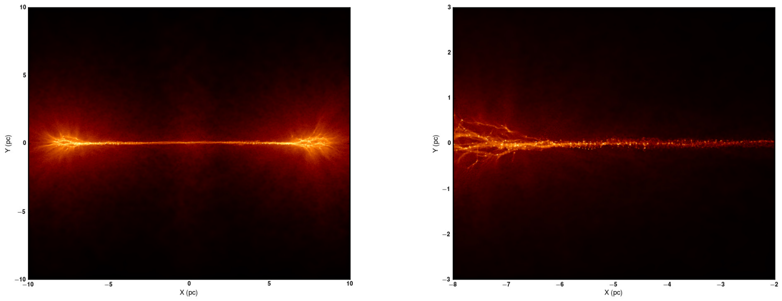

Figure 4.4: The two panels show different regions of the 2 $\mathrm{km\,s^{-1}}$ collision, viewed from the side. The left panel is 10 pc to a side where we are able to see a long filament of dense gas connecting the two clouds. The right panel is a more detailed view, 3 pc to a side, showing the dense clumps in which star formation may occur. The right panel also highlights the filaments in cloud A (left cloud) which are produced by the supersonic turbulent velocity field that are present.

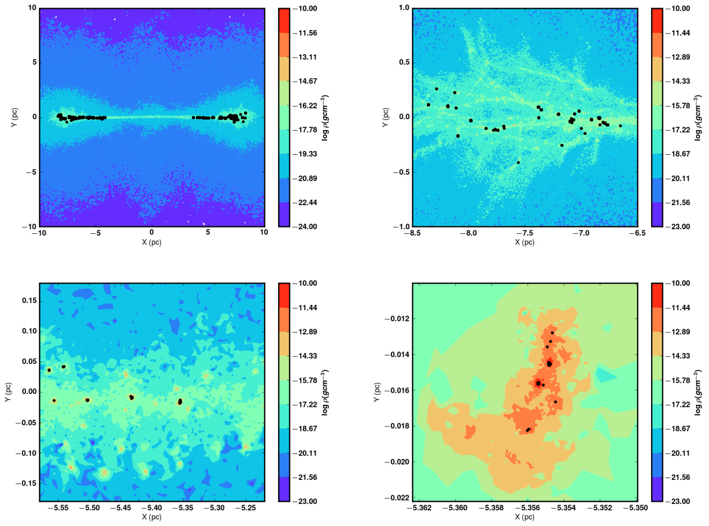

Figure 4.5: Contour maps of the 2 $\mathrm{km\,s^{-1}}$ collision. The Panel goes from most overall view top left to a star cluster view in the bottom right. All panels are in the point of view from the side of the collision (X-Y plane).

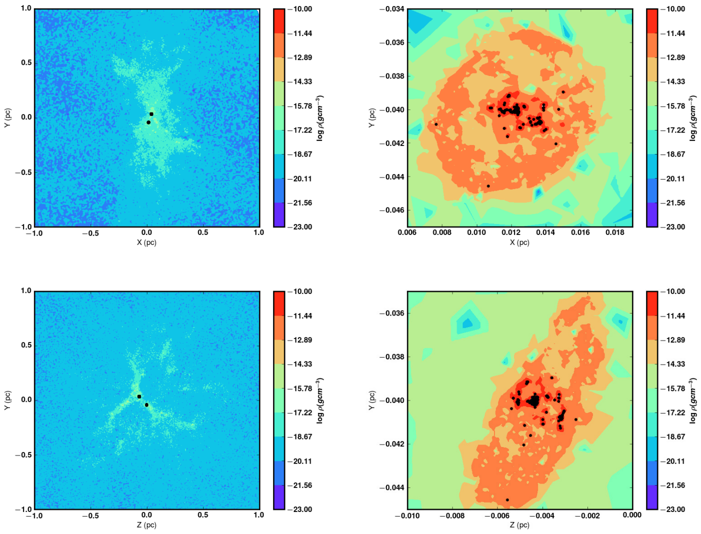

Figure 4.6: Contour maps of the 4 $\mathrm{km\,s^{-1}}$ collision. The two left panels illustrate the overall view of the collision from the X-Y and Y-Z planes. The right two panels highlight specific star clusters, 0.005 pc to a side.

from $X = -0.5$ pc to $X = 0.5$ pc. The 8 $\mathrm{km\,s^{-1}}$ extends to a thickness of about 1.5 pc, from $X = -0.75$ pc to $X = 0.75$ pc. And finally the 10 $\mathrm{km\,s^{-1}}$ has a thickness of 2 pc starting at $X = -1.0$ pc and finishing at $X = 1.0$ pc. Stars form in the densest regions on the plane occurring in areas where density exceed $\rho = 10^{-12}$ $\mathrm{gcm^{-3}}$.

The contour maps highlighting the density of the star forming regions in the collisions are shown in figures 4.6, 4.7, 4.8, 4.9. The left two panels of each of the figures show an overall view of the collisions in both the X-Y, and Y-Z planes. The right two panels show specific star clusters formed in each of the collisions, also viewed in the X-Y and Y-Z planes.

4.2.1 Mass spectrum from the collisions

We compare the mass spectrum produced by each collision to see if there is any influence that the initial velocity has on the spectrum of formed stars. There seems to be a difference between the 2 $\mathrm{km\,s^{-1}}$ collision and the higher velocity collisions, shown in figure 4.11. This may be because the collisions involving velocities greater than 2 $\mathrm{km\,s^{-1}}$ star formation happens after the collision, while in the 2 $\mathrm{km\,s^{-1}}$ case star formation begins before the collision.

To confirm this we performed a two sample Kolmogorov-Smirnov (K-S) test to check the difference in the mass spectrum produced from the low

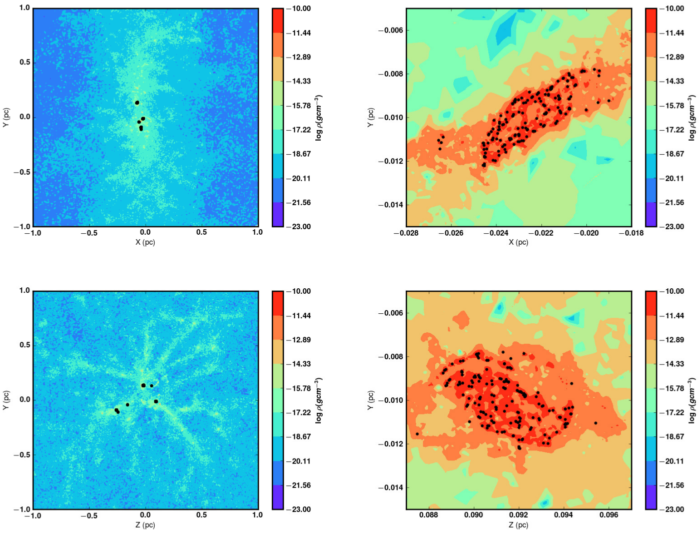

Figure 4.7: Same as figure 4.6, but for the 6 $\mathrm{km\,s^{-1}}$ collision.

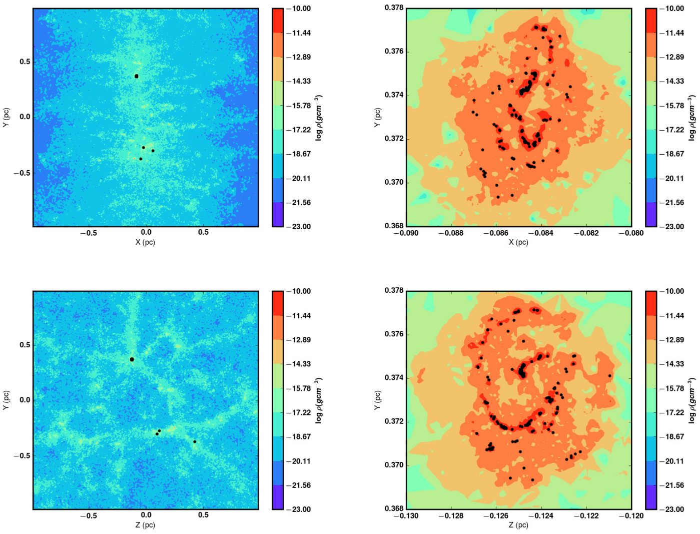

Figure 4.8: Same as figure 4.6, but for the 8 $\mathrm{km\,s^{-1}}$ collision.

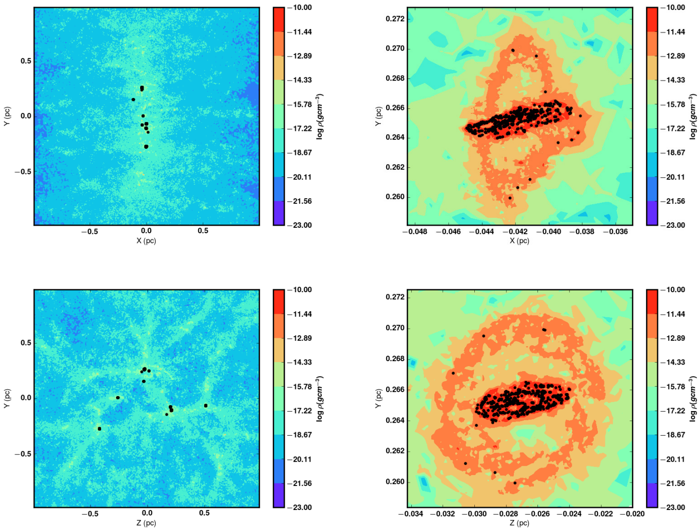

Figure 4.9: Same as figure 4.6, but for the 10 $\mathrm{km\,s^{-1}}$ collision.

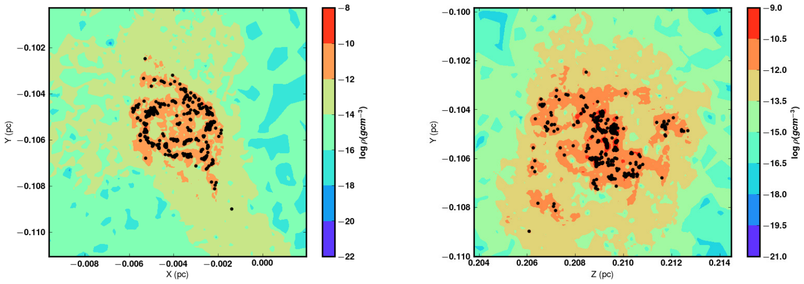

Figure 4.10: A contour map of a star cluster formed from the 10 $\mathrm{km\,s^{-1}}$ collision. In the left panel we view the cluster in the X-Y plane, and in the right panel in the Y-Z plane. The black points are the location of formed stars.

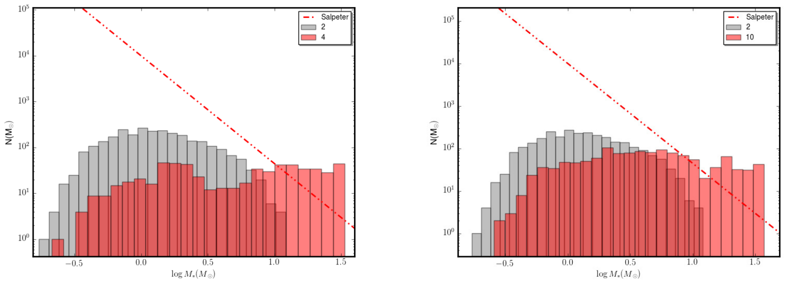

Figure 4.11: In the left panel we see a comparison of mass spectrum between the 2 $\mathrm{km\,s^{-1}}$ collision shown in grey and the 4 $\mathrm{km\,s^{-1}}$ shown in red. In the right panel we see the comparison between 2 $\mathrm{km\,s^{-1}}$ in grey and 10 $\mathrm{km\,s^{-1}}$ shown in red.

velocity collision (2 $\mathrm{km\,s^{-1}}$) with each of the higher velocity (4, 6, 8 and 10 $\mathrm{km\,s^{-1}}$) mass spectra. The results of the test show a p value of 0, which confirms that there is no similarity between the IMF created from the 2 $\mathrm{km\,s^{-1}}$ collision and IMFs created by the 4, 6, 8 and 10 $\mathrm{km\,s^{-1}}$ collisions. Full results of this test are shown in table 4.4.

We also performed a two sample K-S test to check the similarity between each of the higher velocity cases (4, 6, 8 and 10 $\mathrm{km\,s^{-1}}$). The result shows that there is no similarity between the higher velocity cases. We do not observe an overall trend in the mass spectra as collision speed increases. We conclude that this result is due to the stochastic nature of star formation within molecular clouds.

Table 4.4: Results of the 2 sample K-S test. The mass spectrum of the 2 $\mathrm{km\,s^{-1}}$ collision was compared with itself and the higher velocity collisions. The K-S statistic D, is the maximum difference between the two distributions.

Collision [$\mathrm{km\,s^{-1}}$]	D statistic	p value
2	0.0	1.0
4	0.62	0.0
6	0.48	0.0
8	0.56	0.0
10	0.46	0.0

4.2.2 Star clusters

We identified and measured the masses of 24 clusters within the all of the collisions. Each cluster was picked by eye where there exists a separate clump of gas with densities $\rho > 10^{-13}$ gcm^{-3} with an obvious compact population of stars. A good example of clusters we identified can be seen in two right panels of figures 4.6, 4.7, 4.8, 4.9. And another example is the cluster in figure 4.10.

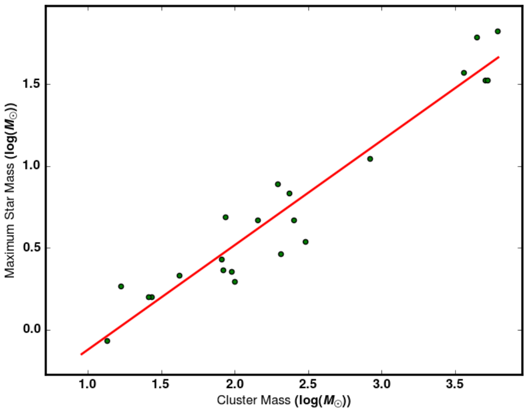

Figure 4.12: The green points are the logarithm of maximum stellar mass in a cluster versus the logarithm the host cluster mass. The red line is a fitted power law with an exponent of 1.

The number of stars in the identified clusters range from ≈ 10 members to 600, with the total cluster mass ranging from $\approx 10M_\odot$ to $6200M_\odot$. In each of the clusters we measured the total mass of the cluster and the maximum stellar mass in each cluster. We notice that there is a linear trend between the logarithm of maximum stellar mass and the logarithm of total cluster mass. Shown in figure 4.12 is fitted a power law with a slope of 1 to our data, which was done through a linear regression that minimized the least squares criterion. We also performed a chi-squared goodness of fit test of the fitted line to our data, that confirms the line is a good fit with a p value of $p = 0.99$. This confirms the trend shown in figure 1.8 which may provide more insight into the upper limit on the maximum possible stellar mass.

Chapter 5

Summary and future work

5.1 Summary

In this thesis we studied the formation of stars from colliding molecular clouds by performing smoothed particle hydrodynamic simulations of six head-on collisions between two molecular clouds. The collisions were given an initial velocity of 0, 2, 4, 6, 8 and 10 $\mathrm{km\,s^{-1}}$ respectively. Each cloud is turbulence supported and marginally bound with radii of $R = 10$ pc and masses of $M = 4.35 \times 10^4 M_\odot$. The two clouds are identical except in their initial supersonic turbulent velocity fields. Each velocity field was populated from a Monte Carlo method which was seeded differently for each cloud. The initial conditions of each cloud were kept the same in each simulation.

We identify the formation of stars in our simulations by a satisfaction of four criteria: density, overlap, velocity divergence, and binding energy criteria. We did not implement a sink creating algorithm during our runs, rather we ran our simulations until significant clumpiness was achieved and analyzed the stellar candidates as the system evolved. This was done to avoid spurious sink creation. The accuracy of the criteria was checked, in chapter 3, by reproducing an initial mass function (IMF) of the formed stars from a single cloud collapse and comparing to the IMF predicted by Saltpeter. We also tested how an increase of mass resolution would populate a mass spectrum with a build up of masses below $2M_\odot$, and a lack in masses above $10M_\odot$.

In section 4.2, we find that in collisions involving initial velocities > 2 $\mathrm{km\,s^{-1}}$ star formation begins after the centers of each cloud have significantly collided. Star formation is initiated earlier as the velocity of the collision increases, while slightly more stars form at lower collision velocities. We observe, in section 4.2.1, a difference in the mass spectra produced from the

2 $\mathrm{km\,s^{-1}}$ collision and the higher velocity collisions (4, 6, 8 and 10 $\mathrm{km\,s^{-1}}$). This is confirmed by performing a 2 sample Kolmogrov-Smirnov test on the mass spectra from the 2 $\mathrm{km\,s^{-1}}$ collision with each of the higher velocity collisions.

Finally in section 4.2.2 we identify 24 star clusters in all of our simulations of colliding molecular clouds. The number of stars in the clusters range from $\approx$ 10 members to 600, with the total cluster mass ranging from $\approx 10M_{\odot}$ to $6200M_{\odot}$. We observed a linear relationship between the logarithm of the maximum stellar mass in the cluster and the logarithm of the host cluster mass.

5.2 Future Work

There are three areas where this research can be developed in the future. The first would be to implement the sink finding algorithm described in chapter 3 into the ChaNGa code. This would allow future SPH simulations of star formation in molecular clouds using ChaNGa to correctly identify and use sinks while the simulation runs. In order to adapt this method we need to implement a correct recipe for accretion of SPH particles onto existing sinks. This would allow the forming stellar systems, identified as sinks, to better evolve with time. These methods are not new to hydrodynamic simulations of star formation, but the implementation of a sink creation and accretion model in into code with better gas treatment like ChaNGa will improve numerical studies of star formation.

Second, we need to give a more robust investigation of the linear trend between the logarithm of maximum stellar mass in a cluster verses the logarithm cluster mass, which was observed in section 4.2.2. This can be done by including current recipes for radiative cooling of planetary systems in our simulations. In each of the simulations in this thesis the evolution of star formation was assumed to be isothermal. This does not properly treat the local variations of the equations of state that might occur between the balance of heating and cooling mechanisms of forming protostellar systems. We can follow the prescriptions used in the research of Boley et al. [7].

Finally we can focus this research on the star formation from molecular cloud collisions in the center of the Milky Way. The origin of young massive stars within the central parsec of the Galactic Center is an open question [17], [30]. Current numerical studies have been put forth to study the phenomenon of star formation in molecular clouds orbiting the Milky Way's central black hole [31]. Also recent observations have confirmed collisions of molecular clouds in the Galactic center involving velocities of $\approx 50\ \mathrm{km\,s^{-1}}$ [46]. We can study star formation by introducing a super-massive black hole particle into our simulations through a collisionless particle of $M_{bh} = 3.5 \times 10^6 M_\odot$ and putting the clouds into orbit around it.

5.2.1 Acknowledgments

I would like to thank Michela Mapelli and Paola Marigo for all of their valuable comments to help me understand the topics in my research. Additionally I would like to thank the ForDyS research group at INAF Padova for all of the support. I am great full for the computational time on the supercomputer Galileo at CINECA along with the Scighera server in the INAF - Astronomical Observatory of Padova. Finally I would like to thank Andrea Rumpold in the Institute for Astro & Particle Physics at the University of Innsbruck for all of the support during the AstroMundus Master Programme.

Bibliography

[1] S. J. Aarseth. Dynamical evolution of clusters of galaxies, I. *Mon. Not. R. Astron. Soc,*, 126:223, 1963.

[2] M. R. Bate and A. Burkert. Resolution requirements for smoothed particle hydrodynamics calculations with self-gravity. *Mon. Not. R. Astron. Soc,*, 288:1060–1072, July 1997.

[3] M. Beech and R. Mitalas. Formation and evolution of massive stars. *ApJS*, 95:517–534, December 1994.

[4] Alejandro Benitez-Llambay. py-sphviewer: Py-sphviewer v1.0.0, July 2015.

[5] E. A. Bergin and M. Tafalla. Cold Dark Clouds: The Initial Conditions for Star Formation. *ARA&A*, 45:339–396, September 2007.

[6] L. Blitz. Giant molecular clouds. In E. H. Levy and J. I. Lunine, editors, *Protostars and Planets III*, pages 125–161, 1993.

[7] A. C. Boley, T. Hayfield, L. Mayer, and R. H. Durisen. Clumps in the outer disk by disk instability: Why they are initially gas giants and the legacy of disruption. *Icarus*, 207:509–516, June 2010.

[8] G. Chabrier. Galactic Stellar and Substellar Initial Mass Function. *PASP*, 115:763–795, July 2003.

[9] David C. Collins, Hao Xu, Michael L. Norman, Hui Li, and Shengtai Li. Cosmological adaptive mesh refinement magnetohydrodynamics with enzo. *The Astrophysical Journal Supplement Series*, 186(2):308, 2010.

[10] F. Combes and G. Pineau des Forets, editors. *Molecular Hydrogen in Space*. Cambridge University Press, 2000. Cambridge Books Online.

[11] D. P. Cox. The Three-Phase Interstellar Medium Revisited. *ARA&A*, 43:337–385, September 2005.

[12] B. D. Crosby, B. W. O'Shea, B. D. Smith, M. J. Turk, and O. Hahn. Population III Star Formation in Large Cosmological Volumes. I. Halo Temporal and Physical Environment. *APJ*, 773:108, August 2013.

[13] T. M. Dame, D. Hartmann, and P. Thaddeus. The Milky Way in Molecular Clouds: A New Complete CO Survey. *APJ*, 547:792–813, February 2001.

[14] A. S. Eddington. *The Internal Constitution of the Stars*. 1926.

[15] C. Federrath, R. Banerjee, P. C. Clark, and R. S. Klessen. Modeling Collapse and Accretion in Turbulent Gas Clouds: Implementation and Comparison of Sink Particles in AMR and SPH. *APJ*, 713:269–290, April 2010.

[16] Y. Fujimoto, E. J. Tasker, and A. Habe. Environmental dependence of star formation induced by cloud collisions in a barred galaxy. *Mon. Not. R. Astron. Soc,*, 445:L65–L69, November 2014.

[17] R. Genzel, F. Eisenhauer, and S. Gillessen. The Galactic Center massive black hole and nuclear star cluster. *Reviews of Modern Physics*, 82:3121–3195, October 2010.

[18] R. Genzel and J. Stutzki. The Orion Molecular Cloud and star-forming region. *ARA&A*, 27:41–85, 1989.

[19] L. Hartmann, J. Ballesteros-Paredes, and E. A. Bergin. Rapid Formation of Molecular Clouds and Stars in the Solar Neighborhood. *APJ*, 562:852–868, December 2001.

[20] D. A. Hubber, S. Walch, and A. P. Whitworth. An improved sink particle algorithm for SPH simulations. *Mon. Not. R. Astron. Soc,*, 430:3261–3275, April 2013.

[21] J. H. Jeans. The Stability of a Spherical Nebula. *Philosophical Transactions of the Royal Society of London. Series A, Containing Papers of a Mathematical or Physical Character*, 199:1–53, 1902.

[22] R. S. Klessen, M. R. Krumholz, and F. Heitsch. Numerical Star-Formation Studies – A Status Report. *ArXiv e-prints*, June 2009.

[23] P. Kroupa, C. A. Tout, and G. Gilmore. The distribution of low-mass stars in the Galactic disc. *Mon. Not. R. Astron. Soc,*, 262:545–587, June 1993.

[24] P. Kroupa and C. Weidner. Evidence for a fundamental stellar upper mass limit from clustered star formation, and some implications therof. In R. Cesaroni, M. Felli, E. Churchwell, and M. Walmsley, editors, *Massive Star Birth: A Crossroads of Astrophysics*, volume 227 of *IAU Symposium*, pages 423–433, 2005.

[25] M. R. Krumholz and J. C. Tan. Slow Star Formation in Dense Gas: Evidence and Implications. *APJ*, 654:304–315, January 2007.

[26] N. Kuno, N. Sato, H. Nakanishi, A. Hirota, T. Tosaki, Y. Shioya, K. Sorai, N. Nakai, K. Nishiyama, and B. Vila-Vilaró. Nobeyama CO Atlas of Nearby Spiral Galaxies: Distribution of Molecular Gas in Barred and Nonbarred Spiral Galaxies. *Publ. Astron. Soc. Jpn.*, 59:117–166, February 2007.

[27] C. J. Lada and E. A. Lada. Embedded Clusters in Molecular Clouds. *ARA&A*, 41:57–115, 2003.

[28] R. B. Larson. Turbulence and star formation in molecular clouds. *Mon. Not. R. Astron. Soc,*, 194:809–826, March 1981.

[29] Mordecai-Mark Mac Low and Ralf S. Klessen. Control of star formation by supersonic turbulence. *Rev. Mod. Phys.*, 76:125–194, Jan 2004.

[30] M. Mapelli and A. Gualandris. Star Formation and Dynamics in the Galactic Centre. In F. Haardt, V. Gorini, U. Moschella, A. Treves, and M. Colpi, editors, *Lecture Notes in Physics, Berlin Springer Verlag*, volume 905 of *Lecture Notes in Physics, Berlin Springer Verlag*, page 205, 2016.

[31] M. Mapelli, T. Hayfield, L. Mayer, and J. Wadsley. In Situ Formation of SgrA* Stars Via Disk Fragmentation: Parent Cloud Properties and Thermodynamics. *APJ*, 749:168, April 2012.

[32] C. Maraston. Evolutionary population synthesis: models, analysis of the ingredients and application to high-z galaxies. *Mon. Not. R. Astron. Soc,*, 362:799–825, September 2005.

[33] P. Massey. MASSIVE STARS IN THE LOCAL GROUP: Implications for Stellar Evolution and Star Formation. *ARA&A*, 41:15–56, 2003.

[34] P. Massey and D. A. Hunter. Star Formation in R136: A Cluster of O3 Stars Revealed by Hubble Space Telescope Spectroscopy. *APJ*, 493:180–194, January 1998.

[35] H. Menon, L. Wesolowski, G. Zheng, P. Jetley, L. Kale, T. Quinn, and F. Governato. Adaptive techniques for clustered N-body cosmological simulations. *Computational Astrophysics and Cosmology*, 2:1, March 2015.

[36] H. W. Moos, W. C. Cash, L. L. Cowie, A. F. Davidsen, A. K. Dupree, P. D. Feldman, S. D. Friedman, J. C. Green, R. F. Green, C. Gry, J. B. Hutchings, E. B. Jenkins, J. L. Linsky, R. F. Malina, A. G. Michalitsianos, B. D. Savage, J. M. Shull, O. H. W. Siegmund, T. P. Snow, G. Sonneborn, A. Vidal-Madjar, A. J. Willis, B. E. Woodgate, D. G. York, T. B. Ake, B.-G. Andersson, J. P. Andrews, R. H. Barkhouser, L. Bianchi, W. P. Blair, K. R. Brownsberger, A. N. Cha, P. Chayer, S. J. Conard, A. W. Fullerton, G. A. Gaines, R. Grange, M. A. Gummin, G. Hebrard, G. A. Kriss, J. W. Kruk, D. Mark, D. K. McCarthy, C. L. Morbey, R. Murowinski, E. M. Murphy, W. R. Oegerle, R. G. Ohl, C. Oliveira, S. N. Osterman, D. J. Sahnow, M. Saisse, K. R. Sembach, H. A. Weaver, B. Y. Welsh, E. Wilkinson, and W. Zheng. Overview of the Far Ultraviolet Spectroscopic Explorer Mission. *APJL*, 538:L1–L6, July 2000.

[37] A. A. Muench, E. A. Lada, C. J. Lada, R. J. Elston, J. F. Alves, M. Horrobin, T. H. Huard, J. L. Levine, S. N. Raines, and C. Romn-Ziga. A study of the luminosity and mass functions of the young ic 348 cluster using flamingos wide-field near-infrared images. *The Astronomical Journal*, 125(4):2029, 2003.

[38] F. Palla and S. W. Stahler. Star Formation in Space and Time: Taurus-Auriga. *APJ*, 581:1194–1203, December 2002.

[39] H. C. Plummer. On the problem of distribution in globular star clusters. *Mon. Not. R. Astron. Soc,*, 71:460–470, March 1911.

[40] William H. Press, Saul A. Teukolsky, William T. Vetterling, and Brian P. Flannery. *Numerical Recipes 3rd Edition: The Art of Scientific Computing*. Cambridge University Press, New York, NY, USA, 3 edition, 2007.

[41] T. S. Rice, A. A. Goodman, E. A. Bergin, C. Beaumont, and T. M. Dame. A Uniform Catalog of Molecular Clouds in the Milky Way. *APJ*, 822:52, May 2016.

[42] E. E. Salpeter. The Luminosity Function and Stellar Evolution. *APJ*, 121:161, January 1955.

[43] L. Spitzer. *Physical processes in the interstellar medium.* 1978.

[44] V. Springel. The cosmological simulation code GADGET-2. *Mon. Not. R. Astron. Soc,*, 364:1105–1134, December 2005.

[45] R. B. Stothers. Upper limit to the mass of pulsationally stable stars with uniform chemical composition. *APJ*, 392:706–709, June 1992.

[46] M. Tsuboi, A. Miyazaki, and K. Uehara. Cloud-cloud collision in the Galactic center 50 km s^{-1} molecular cloud. *Publ. Astron. Soc. Jpn.*, 67:109, December 2015.

[47] C. Weidner and P. Kroupa. Evidence for a fundamental stellar upper mass limit from clustered star formation. *Mon. Not. R. Astron. Soc,*, 348:187–191, February 2004.

[48] Jonathan P. Williams and Lucas A. Cieza. Protoplanetary disks and their evolution. *Annual Review of Astronomy and Astrophysics*, 49(1):67–117, 2011.

[49] McKee C. F.” ”Williams J. P., Blitz L. *Protostars and Planets IV*, volume 97. ed. V. Mannings, A. P. Boss, & S. S. Russell (Univ. of Arizona Press), 2000.

[50] M. G. Wolfire and J. P. Cassinelli. Conditions for the formation of massive stars. *APJ*, 319:850–867, August 1987.

[51] L’vov V.S. ”Zakharov V.E. and Falkovich G.”. *Kolmogorov Spectra of Turbulence 1.* Springer.